Powder Technology 391 (2021) 450–466

Contents lists available at ScienceDirect

Powder Technology

journal homepage: www.elsevier.com/locate/powtec

Numerical simulation of direct shear test on granular materials composed of breakable angular particles: A DEM-XFEM approach

Seyyed Mahdi Seyyedan, Ali Asghar Mirghasemi *, Soheil Mohammadi

School of Civil Engineering, College of Engineering, University of Tehran, Tehran, Iran

ARTICLE INFO

Article history:
Received 7 February 2021
Received in revised form 16 May 2021
Accepted 22 June 2021
Available online 24 June 2021

Keywords:
Direct shear test
Granular material
Particle breakage
Discrete element method
Extended finite element method
Crack propagation

ABSTRACT

A combined DEM-XFEM novel approach is used to simulate the direct shear test on assemblies of breakable two-dimensional angular particles in order to study the macro- and micro-mechanical behavior of granular materials and the effect of particle breakage phenomenon on it. Therefore, the direct shear test simulations are conducted on two different particle assemblies, a breakage-disabled (BD) sample and a breakage-enabled (BE) one, and the results are analyzed and compared. In this approach, the particle assembly under direct shear loading is simulated through DEM, while the fracture within individual particles is modeled using XFEM, in which the Hoek-Brown criterion (HB) and an interaction-integral-based LEFM maximum circumferential tensile stress criterion are utilized to model the crack initiation and its propagation, respectively. Overall, the presented results demonstrate that particle breakage in granular materials reduces the amount of anisotropy, the dilative behavior, and the mobilized friction angle of the sample.

1. Introduction

Direct shear test is a broadly used conventional laboratory test in geotechnical investigations for determining the shear strength parameters of geomaterials. Studying the behavior of geomaterials under the direct shear test is considered quite interesting since not only is there a relatively high anisotropy of stress and strain inside the shear box [1], but also the stress and anisotropy principal directions are changing continuously during the shearing phase [2]. In addition, the direct shear test simulations usually suffer from ambiguity in evaluating shear strength parameters at the failure point [3]. The Discrete Element Method (DEM) is one of the most promising numerical tools for modeling the granular media and many geomaterials like rockfills. Therefore, many studies have been accomplished to develop numerical DEM methodologies that consider the rounded 2D and 3D particles under various loading conditions, such as the direct shear test, which is a broadly used conventional laboratory test in geotechnical investigations [4–16]. This method has even been used to study the behavior of clays [17–20]. However, they cannot sufficiently represent an actual rockfill assembly since their rounded particles have extra rotational freedom and less stress concentration.

One major shortcoming of the DEM numerical implementations is that most of them do not consider the phenomenon of particle breakage that extensively affects the macro- and micro-mechanical behavior of rockfills. To overcome these limitations, DEM has been combined with other numerical methods, such as FEM [21–25], XFEM [26,27], and CFD [28,29].

In the present research, a novel approach that combines DEM and XFEM is utilized to develop a program that numerically simulates direct shear tests on assemblies composed of breakable two-dimensional convex angular rockfill particles, in which a non-local criterion is used to control the crack propagation. The direct shear test simulations on both breakage-disabled (BD) and breakage-enabled (BE) particle assemblies were implemented, and the influence of particle breakage on the macro- and micro-mechanical behavior of rockfills was investigated. Apart from the abovementioned, the novelty of this paper lies also in the modeling of direct shear test on assemblies of 2D angular particles, as well as the investigation of particle breakage in it.

2. A brief review on particle breakage simulations

In addition to numerous laboratory tests [30–35], several DEM-based computational methods have been used to simulate particle breakage in granular media, each of which has its particular approach to particle breakage modeling. One of the most broadly used methods is to consider each particle as a cluster built by bonded rigid circular (in 2D simulations) or spherical (in 3D simulations) sub-particles that can disaggregate during the test [36–44], called the cluster-based method. Because of the rounded shapes of their particles, the foresaid models cannot be applied to sharp-edge granular materials such as rockfills; since angular particle assemblies have more particle breakage than rounded particle assemblies due to their higher stress concentration. However, even with angular sub-particles [45,46], the shapes of

* Corresponding author.
E-mail address: aghasemi@ut.ac.ir (A.A. Mirghasemi).

https://doi.org/10.1016/j.powtec.2021.06.038
0032-5910/

the broken particles were arranged from the beginning; in other words, the probable fracture path of each particle was predetermined, which is the most critical weakness of the mentioned models.

Another common DEM-based approach to simulate particle breakage is the replacement method used by Wang et al. [47]. Based on the aforementioned method, they developed a model in which the particle breakage occurred when the total applied stress of a particle, caused by its contacting particles, exceeded the particle strength. Afterwards, the broken particle was replaced by a number of smaller pieces. It can be said that using the mentioned model is less computationally expensive compared to the cluster-based methods that contain a large number of elements. Nevertheless, their breakage path was defined as a line in the direction of minimum principal stress, crossing the contact with the maximum normal force, which can be considered a relative improvement compared to the previously discussed models.

Harmon et al. [48] presented the first breakage method in which the description of arbitrary particle shapes and breakage surfaces was performed using the level set functions. Nonetheless, they defined the breakage path as a line between the two highest applied contact forces, which is not always true.

One of the pioneering particle breakage studies that presented a numerical model with no prearranged particle breakage paths is the one conducted by Bagherzadeh-Khalkhali et al. [21,22]. They developed a combined DEM-FEM method to simulate breakage in rockfill particles. The previous history of crack propagation (i.e., the crack path and the current location of its tip) is not included in their particle breakage simulations, however. Thus, at the beginning of every computation cycle, all particles, even the already cracked but not broken ones, are considered to be entirely uncracked. In addition, the continuum basis of FEM causes some difficulties in the FE modeling of crack propagation problems as the crack is not allowed to pass through any element of the mesh, so remeshing at each step is inevitable. Therefore, FEM can be considered a suitable tool to model crack and discontinuity growth in problems with a priori known discontinuity path [49–53]. To overcome the mentioned FEM drawbacks, the eXtended Finite Element Method (XFEM) has been developed [54,55].

It should be mentioned that other than the combination of DEM and FEM, some other hybrid approaches have also been proposed to simulate particle breakage in granular materials, e.g., the combined peridynamics (PD) and contact dynamics (CD) computational framework introduced by Zhu and Zhao [56].

A combined DEM-XFEM program has been developed in Raisianzadeh et al. [26,27] studies that can simulate particle breakage in a 2D granular assembly of angular rockfill materials under biaxial compression test by using the Hoek-Brown criterion (HB) to determine both the initiation point and the propagation path of the crack in a particle. The Hoek-Brown criterion is an empirical rock failure criterion that has been widely used to predict the failure of any rock sample [57,58]. Although their proposed XFEM model does not have the classic FEM limitations, simplifying assumptions are used in its fracture criterion to determine the state and the angle at which a pre-initiated crack propagates. Thus, the mentioned model demands extensive calibrations with experimental data to provide consistent results since the Hoek-Brown criterion does not fundamentally include any proper formulation for calculating the angle of crack propagation. Accordingly, the appropriate solution applied in the present study is to use the Hoek-Brown criterion only to determine the state in which a crack initiates; and to consider a fracture-mechanics-based criterion to examine the propagation possibility of any pre-initiated crack and the angle of it.

3. Theoretical aspects and numerical implementations

As mentioned, in this study, a DEM-XFEM code is developed to simulate assemblies of breakable angular particles by conducting the direct shear test on the particle assembly. In this approach, the modeling of particle assembly is fulfilled by the DEM part of the program. Additionally, the particle breakage is modeled through the XFEM code, in which the Hoek-Brown criterion (HB) and an interaction-integral-based LEFM maximum circumferential tensile stress criterion are included in the model to determine the mechanism of crack initiation and its propagation, respectively.

The DEM part of the code is a revised version of the program POLY, which was introduced to simulate assemblies of unbreakable two-dimensional angular particles under biaxial compression test by Mirghasemi et al. [59,60]. Also, the XFEM analysis of particles is performed by improving the program developed by Raisianzadeh et al. [26]. Sections 3.1 and 3.2 briefly review the principles of particle assembly simulation and particle breakage analysis, respectively.

3.1. Particle assembly simulation (the DEM model)

In DEM, the entire granular assembly and its boundaries are motionless at the beginning of the test. The force is applied to the set by moving the boundaries, followed by the contact of the boundary particles with the adjacent particles over the short time interval of Δt. Then other particles are forced to move; so, the force transfers through contacts between the particles. By assuming the particles rigid, the contact force between every two arbitrary particles can be obtained by calculating the overlap area of the two using a contact constitutive model. The effect of different contact laws on the mechanical behavior of assemblies composed of angular particles was previously studied by Mirghasemi et al. [59]. They declared that both the linear and non-linear contact laws show similar macroscopic behavior; accordingly, in the present study, the linear contact law was employed for simplicity. After calculating the applied resultant force of each particle, its acceleration can be determined using Newton's second law. Considering that the acceleration is constant, the velocity and displacement of particles are calculated as well. These procedures are repeated until the out-of-balance forces become almost zero. Fig. 1 shows the process that takes place in each computation cycle of DEM.

3.2. Particle breakage simulation (the XFEM model)

In XFEM, the discontinuity enrichment functions, which are used to define cracked elements so that there is no need to match the mesh with the geometry of the crack, are added to the classic finite element method formulation in general crack propagation problems [54].

In fact, a fracture criterion is the mathematical form of a material fracture theory, which determines the conditions in which solid brittle materials, such as rocks, fail under applied external loads. Although numerous fracture criteria, each valid for a specific material, have been proposed in the literature, all can be classified into two categories: “phenomenological” and “mechanical” [61]. Phenomenological fracture criteria like Mohr-Coulomb and Hoek-Brown, are empirical or analytical methods that determine the occurrence of fracture based on the existing stress field in the specimen. Conversely, mechanical fracture criteria such as Griffith and fracture mechanics models are analytical methods that determine the fracture occurrence from the existing flaws and cracks acting as stress concentrators in the specimen. The first approach does not follow the fracture mechanics principles and may not model the crack propagation mechanism properly in some problems. On the other hand, using the second approach would impose the necessity of a pre-existing crack.

From another perspective, in local criteria (like the Hoek-Brown), the stress state at any integration point of the mesh is controlled against a material strength parameter. Therefore, if the failure criterion is met at any point, a crack initiates at or propagates toward it. It was soon noticed that the before-mentioned local results might become unreliable and mesh-dependent since, in this approach, the behavior of any point is only affected by its own stress state. On the other hand, in non-local models, the fracture behavior of any point can be determined using a non-local criterion (the interaction-integral-based LEFM maximum

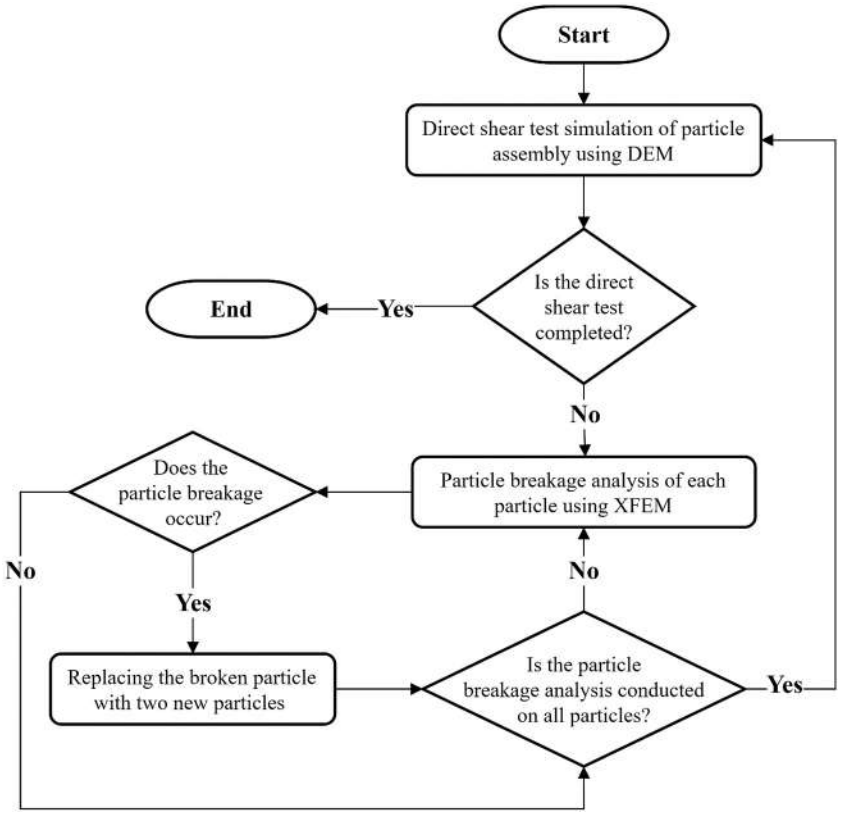

Fig. 1. Flowchart of the algorithm used for DEM-XFEM simulations.

circumferential tensile stress) formulated in terms of the state variables at the aforesaid point and some of its neighboring points [55,62].

Hence, since the application of adequately reliable and straightforward criteria of crack initiation and propagation is crucial in the study of material breakage, in the present research, the Hoek-Brown criterion (HB), from the first approach, and the LEFM maximum circumferential tensile stress criterion, from the second approach, are used to model the crack initiation and its propagation, respectively. Further details on the numerical implementation of the XFEM model and the crack initiation criterion are available in [26]. The proposed crack propagation criterion is presented in Section 3.2.1. In addition, the performance of the developed XFEM model for crack simulation is discussed in Section 3.2.2.

3.2.1. Crack propagation criterion

After selecting a criterion for the crack initiation, an appropriate criterion should also be chosen to determine the possibility of crack propagation and its angle, based on the fracture mechanics principles. In this study, the maximum circumferential tensile stress criterion with an interaction-integral-based linear elastic fracture mechanics (LEFM) approach is employed to accomplish this purpose. First, it is required to review several concepts of classical fracture mechanics.

Eshelby [63,64], during his researches on dislocations in elastic domains, represented some path independent contour integrals by using the theorem of energy conservation. The significance and applicability of this accomplishment in fracture mechanics were not known until Rice and Rosengren [65] realized and stated the importance of the J integral. Considering w_s as the strain energy density, the two-dimensional form of this path independent integral in a problem without the presence of the body force and crack tractions can be represented as follows [55]:

$$J = \oint_{\Gamma} \left(w_s \delta_{1j} - \sigma_{ij} \frac{\partial u_i}{\partial x} \right) n_j d\Gamma \tag{1}$$

$$w_s = \int_0^{\varepsilon_{ij}} \sigma_{ij} d\varepsilon_{ij} = \frac{1}{2} \sigma_{ij} \varepsilon_{ij} \tag{2}$$

$d\Gamma$ is the differential element of the arc along the closed counterclockwise contour Γ, and u_i is the displacement component. In addition, σ_{ij} and ε_{ij} are the stress and strain components on a plane defined by the outward normal vector n, represented by its components n_i, respectively (Fig. 2a). The relation of the J integral with mode I and II stress intensity factors (K_I and K_{II}) and the effective elastic modulus (E') that is equal to the elastic modulus (E) at plane stress condition can be written as [55]:

$$J = \frac{1}{E'} \left({K_I}^2 + {K_{II}}^2 \right) \tag{3}$$

In order to provide an alternative procedure to the primary J integral, Li et al. [66] proposed an approach called the equivalent domain integral method by substituting the contour integral with an equivalent area integral, which is more adapted to FEM-based solutions. According to this method, the J integral can be interpreted as [55]:

$$J = \int_A \left(\sigma_{ij} \frac{\partial u_i}{\partial x_1} - w_s \delta_{1j} \right) \frac{\partial q}{\partial x_j} dA \tag{4}$$

where q is an arbitrary function that is equal to 1.0 and 0.0 on Γ3 and Γ1 domain boundaries, respectively (Fig. 2b); also, domain A represents the area enclosed between the interior contour Γ3 and the exterior contour Γ1.

Additionally, the J integral can be determined by a modified equivalent domain integral approach called the interaction integral method in which the auxiliary state (aux) is chosen so that both the traction-free boundary condition on the crack surface and the equilibrium equation are satisfied in domain A. Thus, considering w^M as the interaction work, the interaction integral (M) is defined as follows [55]:

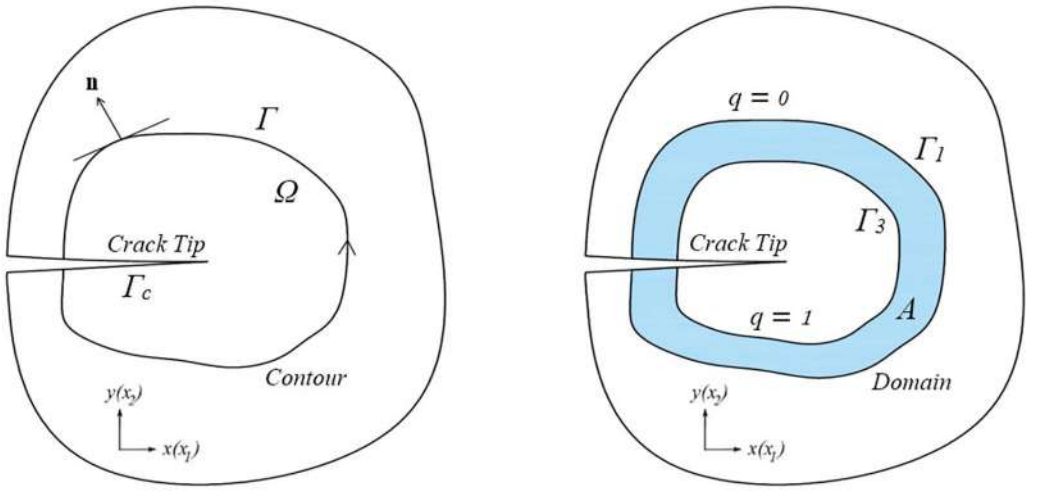

(a) Contour around the crack tip (b) Equivalent domain around the crack tip

Fig. 2. Schematic of J integral definition in crack problems.

$$M = \int_A \left(\sigma_{ij} \frac{\partial u_i^{aux}}{\partial x_1} + \sigma_{ij}^{aux} \frac{\partial u_i}{\partial x_1} - w^M \delta_{1j} \right) \frac{\partial q}{\partial x_j} dA \tag{5}$$

$$w^M = \frac{1}{2} \left(\sigma_{ij} \varepsilon_{ij}^{aux} + \sigma_{ij}^{aux} \varepsilon_{ij} \right) \tag{6}$$

In a similar way to Eq. (3), the relation of the M integral with mode I and II stress intensity factors (K_I and K_{II}) can be formulated as [55]:

$$M = \frac{2}{E'} \left(K_I K_I^{aux} + K_{II} K_{II}^{aux} \right) \tag{7}$$

By selecting appropriate auxiliary fields in the M integral calculation, the values of K_I and K_{II} can be computed using Eq. (7). Therefore, by considering the auxiliary field as a pure Mode I loading condition, in which $K_I^{aux} = 1$ and $K_{II}^{aux} = 0$, the value of K_I is computed. In the same way, to calculate K_{II}, the auxiliary field can be assumed to be a pure Mode II loading condition with $K_I^{aux} = 0$ and $K_{II}^{aux} = 1$. Hence, in either case, the stress intensity factor is obtained from [55]:

$$K = \frac{E'}{2} M \tag{8}$$

Moreover, to determine the parameters of the auxiliary field, the analytical solution of Westergaard [67] for the plane stress crack problem is adopted [68]:

$$\sigma_{11}^{aux} = \frac{1}{\sqrt{2\pi r}} \left\{ K_I^{aux} \mathrm{Cos}\left(\frac{\theta}{2}\right) \left[1 - \mathrm{Sin}\left(\frac{\theta}{2}\right) \mathrm{Sin}\left(\frac{3\theta}{2}\right) \right] - K_{II}^{aux} \mathrm{Sin}\left(\frac{\theta}{2}\right) \left[2 + \mathrm{Cos}\left(\frac{\theta}{2}\right) \mathrm{Cos}\left(\frac{3\theta}{2}\right) \right] \right\} \tag{9}$$

$$\sigma_{22}^{aux} = \frac{1}{\sqrt{2\pi r}} \left\{ K_I^{aux} \mathrm{Cos}\left(\frac{\theta}{2}\right) \left[1 + \mathrm{Sin}\left(\frac{\theta}{2}\right) \mathrm{Sin}\left(\frac{3\theta}{2}\right) \right] + K_{II}^{aux} \mathrm{Sin}\left(\frac{\theta}{2}\right) \mathrm{Cos}\left(\frac{\theta}{2}\right) \mathrm{Cos}\left(\frac{3\theta}{2}\right) \right\} \tag{10}$$

$$\sigma_{12}^{aux} = \frac{1}{\sqrt{2\pi r}} \left\{ K_I^{aux} \mathrm{Sin}\left(\frac{\theta}{2}\right) \mathrm{Cos}\left(\frac{\theta}{2}\right) \mathrm{Cos}\left(\frac{3\theta}{2}\right) + K_{II}^{aux} \mathrm{Cos}\left(\frac{\theta}{2}\right) \left[1 - \mathrm{Sin}\left(\frac{\theta}{2}\right) \mathrm{Sin}\left(\frac{3\theta}{2}\right) \right] \right\} \tag{11}$$

$$u_1^{aux} = \frac{1}{2G} \sqrt{\frac{r}{2\pi}} \left\{ K_I^{aux} \mathrm{Cos}\left(\frac{\theta}{2}\right) [\kappa - \mathrm{Cos}(\theta)] - K_{II}^{aux} \mathrm{Sin}\left(\frac{\theta}{2}\right) [\kappa + 2 + \mathrm{Cos}(\theta)] \right\} \tag{12}$$

$$u_2^{aux} = \frac{1}{2G} \sqrt{\frac{r}{2\pi}} \left\{ K_I^{aux} \mathrm{Sin}\left(\frac{\theta}{2}\right) [\kappa - \mathrm{Sin}(\theta)] - K_{II}^{aux} \mathrm{Cos}\left(\frac{\theta}{2}\right) [\kappa - 2 + \mathrm{Cos}(\theta)] \right\} \tag{13}$$

where r and θ are the radial distance and the polar angle measured from the crack tip, respectively. In addition, ν is the Poisson's ratio, G is the shear modulus and equals $E/2(1+\nu)$, and κ is defined as $(3-\nu)/(1+\nu)$.

In order to investigate the possibility of crack propagation in mixed-mode problems, various analytical criteria have been proposed [68], among which the maximum circumferential tensile stress criterion, developed by Erdogan and Sih [69], is used in the present study. In this criterion, the crack propagates radially from its tip inside a plane perpendicular to the direction of maximum tension as the maximum circumferential tensile stress (σ_θ^{max}) reaches a critical material constant. By this assumption, the crack propagation angle (α_c) can be obtained from [68]:

$$\alpha_c = 2\mathrm{Arctan}\left[\frac{1}{4} \left(\frac{K_I}{K_{II}} - sign(K_{II}) \sqrt{\left(\frac{K_I}{K_{II}} \right)^2 + 8} \right) \right] \tag{14}$$

Moreover, an equivalent stress intensity factor (K_{eq}) for mixed-mode problems is defined as [68]:

$$K_{eq} = K_I \left[\mathrm{Cos}\left(\frac{\alpha_c}{2} \right) \right]^3 - \frac{3}{2} K_{II} \mathrm{Cos}\left(\frac{\alpha_c}{2} \right) \mathrm{Sin}(\alpha_c) \tag{15}$$

It is one of the fundamental principles of linear elastic fracture mechanics (LEFM) that when the equivalent stress intensity factor (K_{eq}) reaches its critical value (K_{IC}), unstable fracture happens [68]. K_{IC}, also called mode I fracture toughness, is a material constant that determines the ability of the material to resist a given stress field intensity at the crack tip and prevent progressive tensile crack propagation. Hence, in the present study, the crack propagates under mixed-mode, whenever the stress intensity factor K_{eq} reaches the material mode I fracture toughness K_{IC}.

3.2.2. XFEM model verification

A classic fracture mechanics example is simulated by the XFEM part of the developed program to compare the numerically computed stress intensity factor (K_I) to the one calculated from Irwin's exact analytical solution [70]. The analytical stress intensity factor (K_I) and the

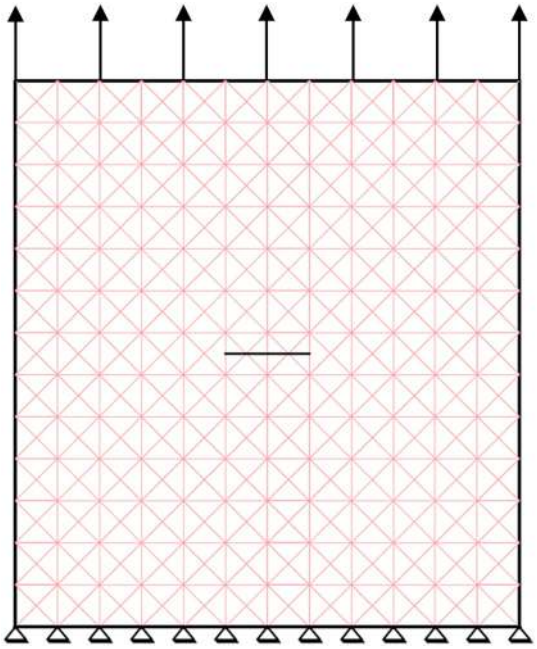

Fig. 3. Numerical simulation of a tensile plate with a central crack for verification of the XFEM model.

Table 1
Normalized values of stress intensity factors.

$\frac{a}{b}$	Irwin $\overline{K}_I$	Coarse mesh		Fine mesh	
		$\overline{K}_I$	Error (%)	$\overline{K}_I$	Error (%)
1/4	1.189	1.167	1.84	1.178	0.92
1/6	1.075	1.052	2.14	1.064	1.02

normalized stress intensity factor ($\overline{K}_I$) for the problem of a finite tensile isotropic rectangular plate of width b with a central crack of length a, shown in Fig. 3, can be defined as [54]:

$$K_I = \overline{K}_I \sigma_0 \sqrt{\pi a} = \overline{K}_I \sigma_0 \sqrt{\pi a} \tag{16}$$

$$\overline{K}_I = \sqrt{\sec \frac{\pi a}{b}} = \left[1 + 0.256\left(\frac{a}{b}\right) - 1.152\left(\frac{a}{b}\right)^2 + 12.2\left(\frac{a}{b}\right)^3\right] \tag{17}$$

The considered plate is discretized by two different meshes of linear triangular elements to evaluate the accuracy of results, a coarse mesh, and a fine one. According to Table 1, the comparison of the normalized stress intensity factors for the aforesaid meshes in different crack length to plate width ratios (a/b) shows an acceptable agreement between the numerical results and the Irwin's solution.

The Brazilian (indirect tensile) test, which is one of the conventional laboratory methods for indirectly determining the tensile strength of brittle materials like rock samples, is based on the failure of a thin disc specimen loaded by a uniform line compression load radially applied at each end over the circumference of the disk. Thus, a standard Brazilian test on a sample with a diameter of 50 *mm* and a thickness of 25 *mm* (thickness-to-diameter ratio of 0.5) [71] is numerically simulated by the present model, in which the disc sample is modeled as its inscribed regular 16-sided polygon since the model is developed for angular particles. The propagated crack path, cracked elements, and the enriched nodes in a simulated Brazilian test specimen are shown in Fig. 4. The figure reveals that, in the same way as the results of experimental observations [72,73], the specimen is split into two pieces as the crack propagation occurred almost in line with the direction of the applied external load.

Table 2 presents the average values of experimental data of the Brazilian tensile strength (*BTS*) and uniaxial compressive strength, reported in the literature [74], for some types of rock; additionally, the numerical simulation results of *BTS* in each sample were provided. However, other than uniaxial compressive strength, the other necessary input parameters of the present model, i.e., the elasticity modulus (E), Poisson's ratio (ν), Hoek-Brown parameter (m_i), and Fracture Toughness (K_{IC}), were not directly measured or reported in most experimental Brazilian tests on rock samples. Thus, the aforesaid parameters for each rock type were determined based on the estimations and suggestions of [75–79]. Finally, According to Table 2, there is a good agreement between the numerical results and the experimental data.

Altogether, the examples mentioned above show that the proposed model can adequately simulate the crack and breakage in rock specimens.

4. Numerical simulations

Fig. 5 shows the direct shear test simulation steps of the breakable and unbreakable particle assemblies in the developed program. First, in the assembly generation phase, apart from defining the body of the shear box (the boundary particles), a set of about 1000 convex angular particles with the desired shapes (in 20 different geometries), dimensions, and distribution is made (Fig. 5a). According to the ASTM D3080–04 standard [80], in the direct shear test, the sample length-to-height ratio in cubic boxes should be at least 2 to 1 (18 m to 9 m, in the present research), and the size of the mentioned shear box should be at least 10 times the diameter of the largest tested particle. Afterwards, by applying hydrostatic stress to the boundaries, all particles move toward the center of the set so that the assembly is compacted. After that, the boundaries are forced to be fixed in their position, and particles are allowed to move only under the influence of their velocities and the forces between them to minimize the inter-particle contacts (Fig. 5b). At the next step, called the assembly vertical confinement phase, the horizontal top boundary particle motion rate is controlled so that the amount of vertical stress, which performs as the direct

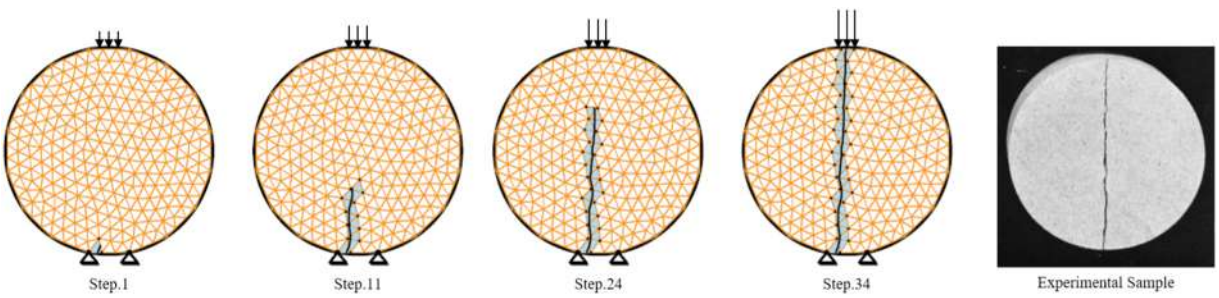

Fig. 4. Simulated Brazilian test sample in different cracking steps compared with a typical experimental broken specimen [73].

Table 2
Comparison of BTS between the present numerical results and the experimental data.

Rock type	Elasticity modulus	Poisson's ratio	HB parameter	Reported UCS	Fracture toughness	Reported BTS	Numerical BTS
	E (GPa)	ν	m_i	σ_{ci} (MPa)	K_{IC} $(MPa.\sqrt{m})$	σ_t (MPa)	σ_t^N (MPa)
Granite	51.0	0.20	29.0	170.3	0.85	10.3	10.61
Limestone	38.5	0.25	12.0	76.9	0.93	6.0	6.24
Marble	30.0	0.25	10.0	10.1	0.15	10.1	9.65
Sandstone	20.0	0.24	13.0	105.3	1.18	9.5	9.68

shear test vertical stress, reaches its desired value (Fig. 5c). At the last step of the test, called the assembly lateral displacement phase, a lateral displacement is applied at a constant rate to the upper half of the shear box. During this process, the amount of assembly vertical stress is being kept constant by the vertical movement of the horizontal top boundary of the shear box. The test continues to the relative lateral displacement (RLD) levels of about 18% (Fig. 5d).

In the present model, the numerical simulations were conducted under vertical stress of 2.0 *MPa*. The preparation of the particle assemblies was so that all of the test specimens had the identical void ratio (e) of 0.2 at the beginning of the lateral displacement phase. A set of parameters were also defined; the values considered for each can be noticed in Table 3. Due to the qualitative nature of this study, the values of these parameters were chosen based on experience. The direct shear test simulations were conducted on two different samples; in one, the breakage was disabled in the particles (BD), and in the other, particle breakage was enabled (BE). However, all other parameters were considered to be the same in these two samples to make it possible to make a valid comparison between them.

5. Results and discussion

In this Section, after explaining the macro-mechanical behavior of BD and BE angular particle assemblies and the effect of particle breakage on the results in Section 5.1, Section 5.2 demonstrates the microscopic observations of these cases.

5.1. Macro-mechanical behavior of the particle assembly

By considering the particle assemblies presented in Fig. 6, the range of the distribution of broken particles, distinguished by red color, at the end of the test can be examined. A diagonal trend of particle breakage was seen in the shear box. Also, the frequency of broken particles in the middle third of the box was significantly higher than the lower and the upper ones. Furthermore, it can be recognized that the newly generated particles in the BE assembly filled the existing pore spaces between the present particles.

Fig. 7a demonstrates the granulation curves of both BD and BE samples at the end of the test. As can be perceived, new smaller particles emerged by the breakage of some larger particles in the assembly. Accordingly, the weight percentage of the smaller particles in the sample increased, which led to a slight decrease in the average size of the assembly particles. Thus, the phenomenon of particle breakage caused the granulation curve to be shifted to the left.

According to the curves of assembly void ratios (e) versus the relative lateral displacement of the upper half of the shear box in Fig. 7b, the particle assemblies showed contractive behaviors at the first steps of the lateral displacement phase; then the dilative behavior continuously dominated. Hence, both samples initially became slightly denser because of the reduction of their empty spaces, and after that, their density decreased as particles came out of these spaces. In addition, by comparing the trend of void ratio changes of the mentioned samples, it is observed that due to particle breakage in the breakable sample (BE), new particles with smaller sizes than the primary particles were created. As well as reducing the amount of interlocking between the particles, these mentioned new particles reduced the volume and porosity of the sample by placing in the empty spaces between the particles of the set. Therefore, the dilative behavior of the BE sample was reduced because of the particle breakage.

Fig. 7c and d represents the curves of horizontal (σ_{11}) and shear (σ_{12}) stresses versus the relative lateral displacement of the upper half of the shear box. As shown, the upward trend of the horizontal stress (σ_{11}) curve stopped at the RLD of about 4%. Also, it can be said that in both BD and BE samples, the shear stress (σ_{12}) increased until reaching

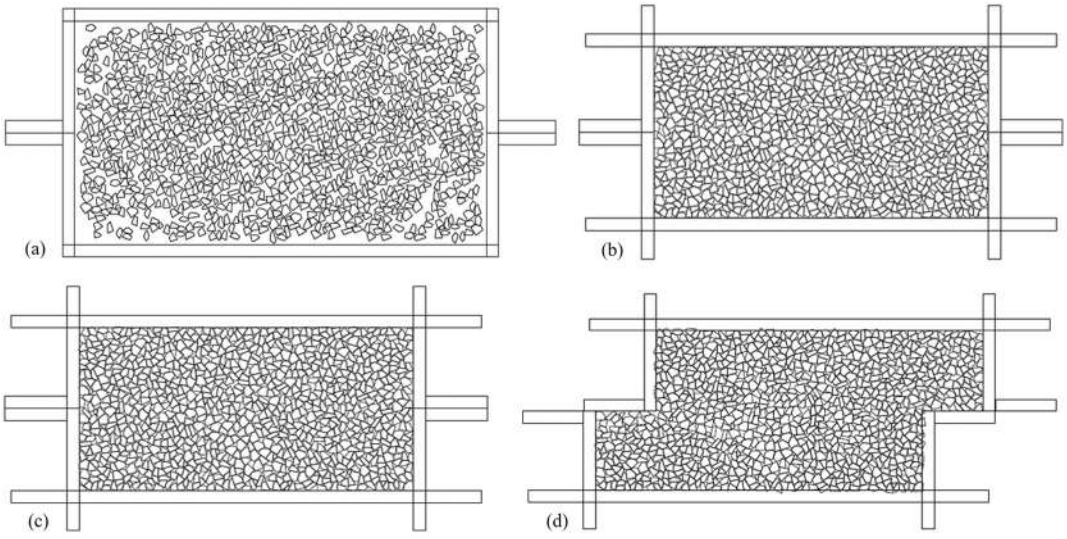

Fig. 5. Assembly of particles in the shear box: (a) after the assembly generation phase; (b) after the compaction and relaxation phase; (c) after the vertical confinement phase; (d) after the lateral displacement phase.

Table 3
Parameters used in simulations of the direct shear test in the present study.

Analysis	Parameter	Value
DEM analysis	Particles Density (ρ)	2500 kg/m^3
	Normal & Tangential Stiffness (K_N, K_S)	2.0×10^7 N/m
	Inter-Particle Friction Coefficient (μ)	0.6
	Wall-Particle Friction Coefficient (μ')	0.4
	Relative Lateral Displacement Rate (Δ_{RLD})	0.005
XFEM analysis	Elastic Modulus (E)	20 GPa
	Poisson's Ratio (ν)	0.2
	Uniaxial Compressive Strength (σ_{ci})	30 MPa
	Hoek-Brown Parameter (m_i)	25
	Fracture Toughness (K_{IC})	0.2 $MPa.\sqrt{m}$

a peak value at the RLD of about 4%; then, it decreased gradually to a residual amount at the end of the direct shear test. As seen, particle breakage reduced the stress state in the assembly by decreasing the interlocking between the particles. Accordingly, given the equal amount of vertical stress (2 *MPa*) in the two samples, a lower mobilized friction angle can be expected from the BE particle assembly. It can be observed that the macroscopic results were qualitatively consistent with conventional experimental direct shear test observations [81].

It can be stated that the presence of a crack in a particle reduces the stiffness of the cracked elements based on the XFEM. However, as long as the particle is not broken, the mentioned crack does not have any considerable global influence on the assembly of particles. Fig. 8 shows the process of particle cracking and particle breakage of the BE assembly during the lateral displacement phase of the direct shear test as curves of the percentage of cracked particles (*Cr%*) and the percentage of particle breakage (*Br%*) versus the *RLD*. As can be seen, the rate (slope of the curve) of particle cracking at the first steps was very high and decreased slightly as the lateral displacement continued. On the other hand, the particle breakage rate was almost uniform (with a slight slope reduction) during the test. In the present study, the cracking of a particle not necessarily leads to its breakage. Therefore, despite the high rate of crack initiation in particles at the early stages of the lateral displacement, particle breakage occurred at an almost uniform rate. Additionally, the gradual increase of broken particles reduced the stress concentration levels in the assembly; thus, the crack initiation rate decreased in the remaining particles. Nonetheless, a small slope drop can be seen in the particle breakage curve during the test. In fact, in the beginning, a significant number of particles broke as they could not move freely under the influence of the load. As the test continued, the particle arrangement of the set became more uniform, and so the particle breakage rate decreased.

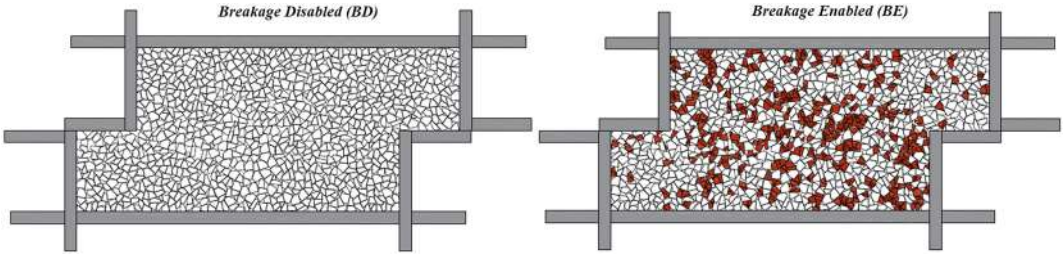

Fig. 6. Assemblies of particles in the shear box after the lateral displacement phase (at the end of the test).

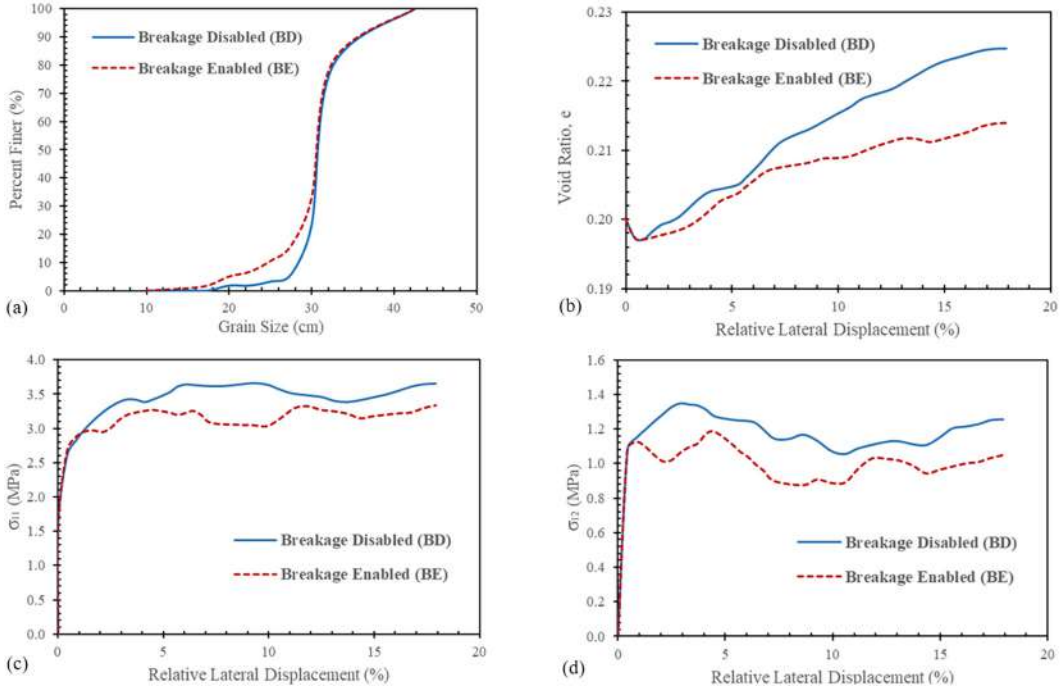

Fig. 7. Macroscopic results of the direct shear test for both BD and BE assemblies.

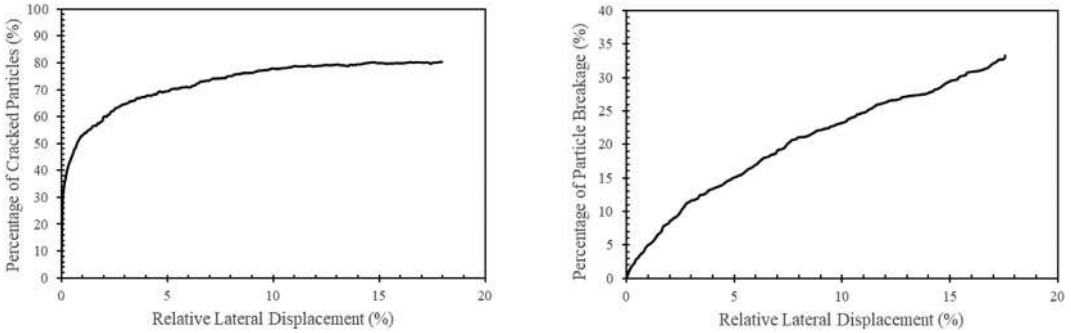

Fig. 8. Variation in the percentage of cracked particles and the percentage of particle breakage for the BE assembly during the lateral displacement phase of the direct shear test.

5.2. Micro-mechanical behavior of the particle assembly

Studying the diagrams of horizontal and vertical displacement of particles during the test results in a deeper understanding of the micro-mechanical behavior of the particle assembly.

As shown in Fig. 9, in both samples, the particles in the lower third of the shear box experienced less horizontal displacement than those placed in the middle and the upper ones. As a matter of fact, the upper third particles moved horizontally in sync with the lateral displacement applied to the boundaries. Also, the particles of the lower third did not tend to move horizontally due to the motionlessness of their boundaries. Meanwhile, some particles in the middle of the shear box formed a hypothetical layer and experienced a range of horizontal displacements from zero (at the lower bound of the assumed layer) to near the maximum lateral displacement (at the upper bound of the assumed layer). These observations can be attributed to forming an area in the middle of the box called the shear band.

By studying the horizontal particle displacements along the height of the box (Fig. 10), it is seen that the decrease of the horizontal particle displacements from the maximum value at the top of the box to the near-zero levels at the bottom of it was more gradual in the BE sample than in the BD one, based on the slopes of the best fit lines. In fact, the reduction of empty spaces between the particles in the BE assembly caused their more uniform horizontal motion. Also, the number of broken particles in the set was almost higher in the shear band area, where there was a greater horizontal particle displacements gradient (relative horizontal displacement between adjacent particles).

Fig. 11 shows that in both assemblies, the particles in the middle of the box experienced higher vertical displacements than the other ones. Since the upper horizontal boundary was free against vertical movement due to the set volume change, vertical particle displacements in the upper half of the box were higher than those of the lower half. It is in accordance with macroscopic observations corroborating the dependence of dilative and compressive behaviors on the loading direction, which is addressed in newly developed constitutive models [82]. Moreover, the results demonstrate that the number of particles with positive vertical displacement (upward) was more than those with negative vertical displacement due to the mostly dilative behavior of both assemblies. In other words, the average dilation of the shear band area was higher than that of the whole assembly. In fact,

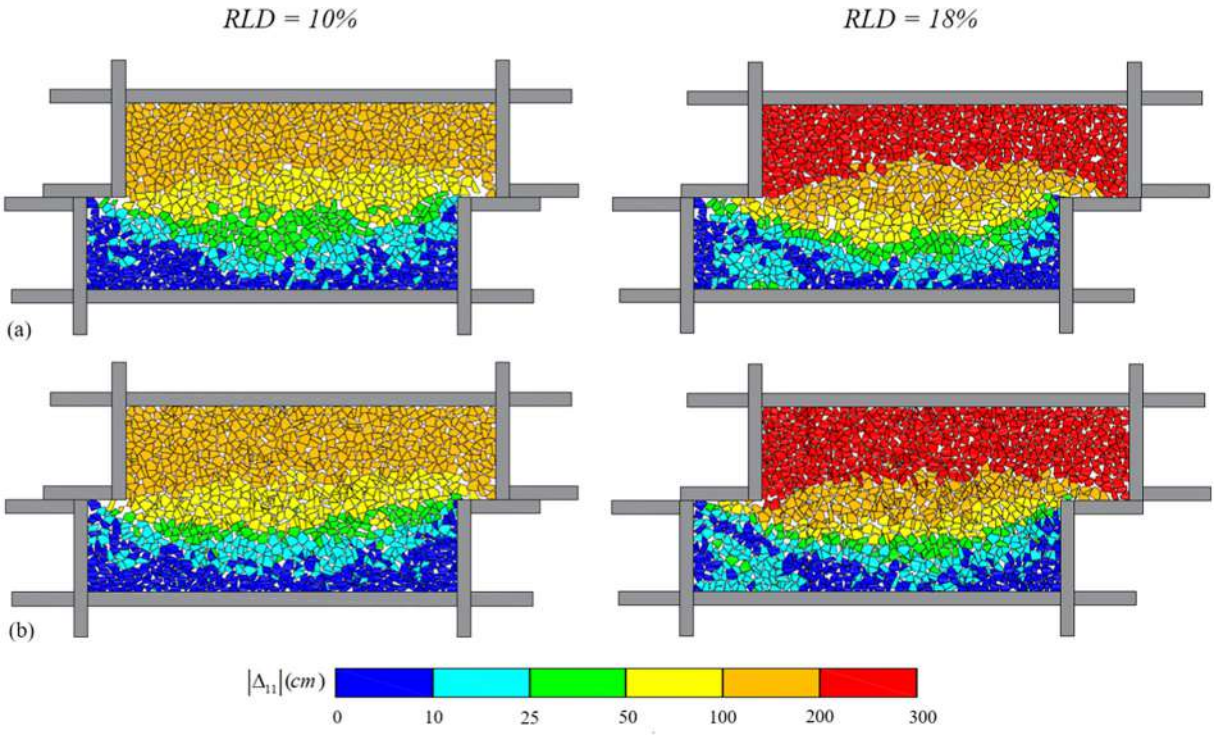

Fig. 9. Contour of horizontal particle displacements (Δ_{11}) during the lateral displacement phase of the direct shear test for: (a) the BD assembly; (b) the BE assembly.

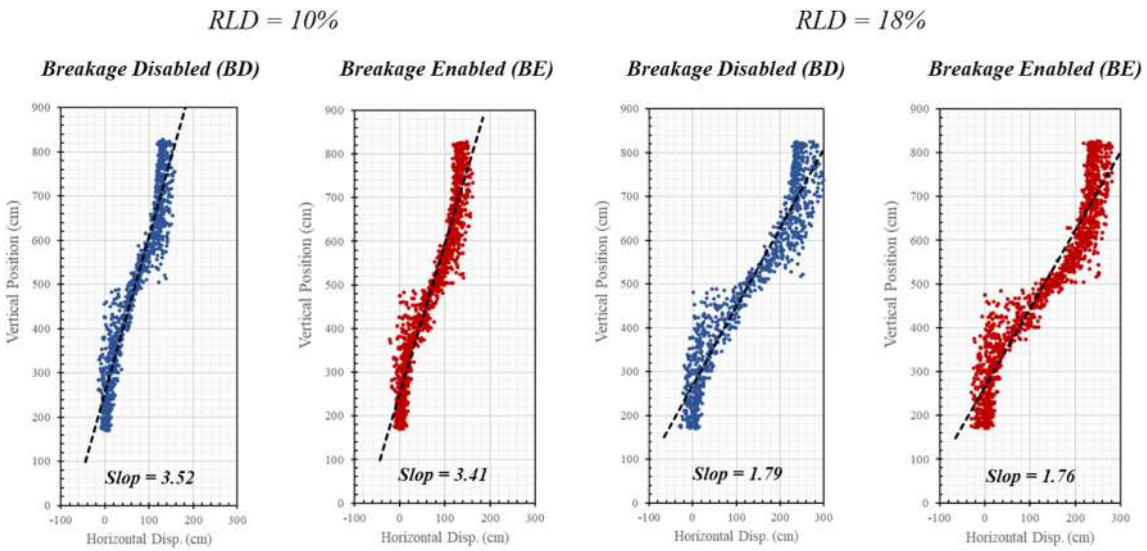

Fig. 10. Variation in horizontal particle displacements (Δ_{11}) along the height of the shear box for both BD and BE assemblies during the lateral displacement phase of the direct shear test.

during the last phase of the test, the porosity of the shear band area was higher than the average porosity of the entire set; therefore, measuring the dilation across the boundaries is not an accurate representation of the dilative behavior of the shear band. Zhang and Thornton [5] have proposed using shear boxes with a higher length-to-height ratio to solve this problem. Additionally, as seen, the broken particles were relatively more in number in the areas where there were high vertical particle displacements.

The comparison of the vertical displacement of particles in the two samples showed that by the occurrence of particle breakage in an assembly, its dilative behavior decreases, and its contractive behavior increases. As a result, the vertical particle displacements were more uniform in the BE sample than those in the other set, based on their standard deviation (SD). The reason was the large number of particle breakages in the middle of the box, where previously accounted as the area with the largest share of the total dilation of the set.

Another form of particle deformation in granular media is rotation. Based on the relative particle rotation contours presented in Fig. 12, it can be recognized that after the vertical confinement phase, there was no particular trend in the distribution of relative particle rotations. However, by applying the lateral displacement, the average relative particle rotation of the assembly ($\Delta\theta_{ave}$) increased, although the relative rotation of particles adjacent to the boundaries decreased. At this stage, the highest relative rotations were observed among the particles at the middle of the shear box. Studies have also shown that relative particle rotation is a useful parameter in determining the shear band, which can be observed in Fig. 12. Furthermore, the average relative particle rotation of the BE assembly was higher than that of the BD sample, as the newly generated particles rotated more freely due to their smaller sizes. On the other hand, the distribution of relative particle rotations was more uniform in the BE sample.

To consider the mechanism in which the contact forces transfer through the particles, the normal and contact force chains for both BD and BE samples during the test are shown in Fig. 13. For depicting these forces symbolically, each contact force was simplified and drawn as a line between the centers of the two particles. Other than the

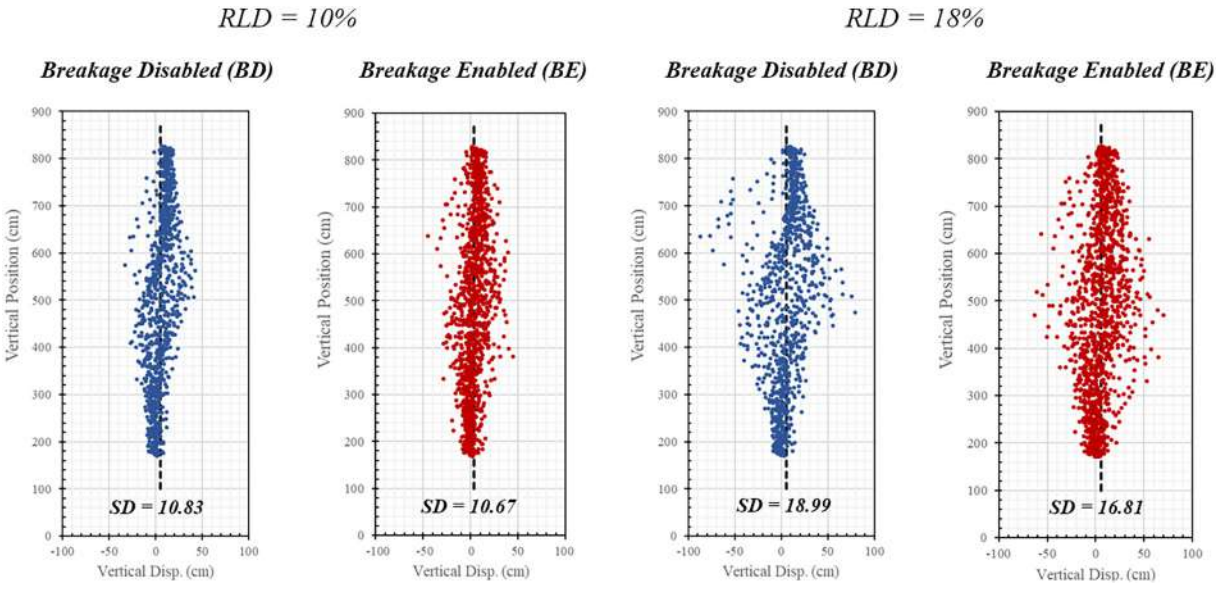

Fig. 11. Variation in vertical particle displacements (Δ_{22}) along the height of the shear box for both BD and BE assemblies during the lateral displacement phase of the direct shear test.

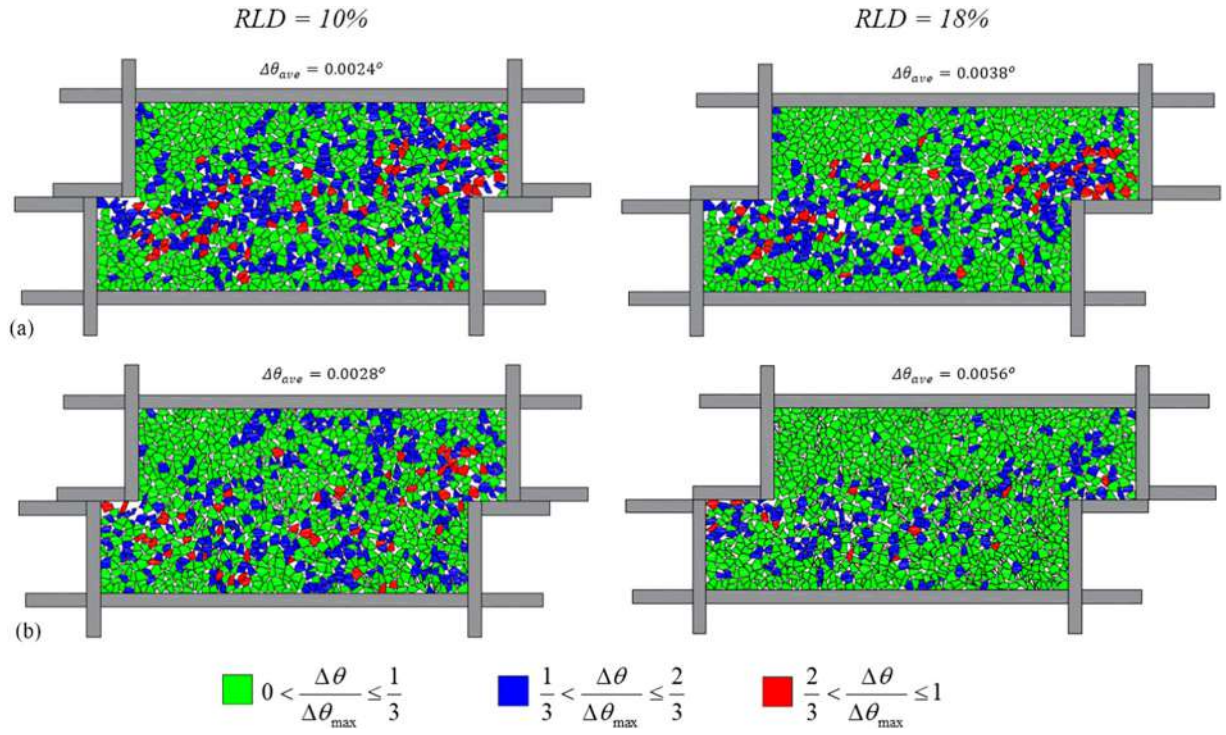

Fig. 12. Contour of particle rotations ($\Delta\theta$) during the lateral displacement phase of the direct shear test for: (a) the BD assembly; (b) the BE assembly.

thickness changing of the contact force lines corresponding to the amount of each contact force, the contact forces were divided with the color into three categories: strong (red lines), medium (blue lines), and weak (green lines). It can be seen that the contact force chains between the angular particles are more complicated than those between the rounded particles [8].

As noticed, the contact force chains were uniformly distributed in the assemblies at the RLD of zero; then, the mentioned uniform distribution gradually disappeared due to lateral left to right displacement. During this process, the particles on the left side of the upper half of the box and those on the right side of the lower half experienced a great number of inter-particle contacts. Thus, the general force flow path in both samples was formed from the upper-left area of the box to its lower-right corner. Also, in both samples, the number of medium and strong inter-particle contact forces increased until the RLD reached about 4%, which is approximately equivalent to the maximum shear strength of the assembly; afterwards, it gradually decreased as these chains started to break.

To quantitatively demonstrate the differences between the normal force chain contours of Fig. 13, the number of strong contact forces was measured in three RLD stages for both BD and BE samples during the test (Table 4). The mentioned data confirms the previously stated observations. As shown in Table 4, the number of strong forces increased during the relative lateral displacement until peak shear strength and then decreased slightly until the end of the test. Moreover, the occurrence of particle breakage in the BE sample decreased the number of its strong contact forces at any RLD stage during the test.

Moreover, the degree of homogeneity of the assembly contact forces can also be quantified by a parameter called the participation number (Γ), calculated as follows [83,84]:

$$\Gamma = \left(N\sum_{i=1}^{N} {q_i}^2\right)^{-1}, \quad q_i = f_i \Big/ \sum_{j=1}^{N} f_j \tag{18}$$

where f is the magnitude of the contact force, and N is the total number of assembly contact forces. Based on the mentioned equation, $q_i = 1/N$ for all q_i follows by $\Gamma = 1$, and represents a state with a complete homogeneous contact force distribution; on the other hand, at the complete non-uniform contact force distribution state $\Gamma \approx 1/N$, which is approximately zero due to the high value of N.

As can be seen in Table 4, the high relatively participation number of the assemblies with relatively homogeneous contact force distribution at the beginning of the lateral displacement phase, decreased until the RLD of 4%. At this stage, which is approximately equivalent to the maximum shear strength of the assembly, the contact force distribution is very non-uniform. Subsequently, the assembly participation number of the samples slightly increased until the test ends. Additionally, at any RLD, the participation number of the BE sample was higher than that of the BD sample as the distribution of contact forces became more uniform due to the particle breakage. It can be seen that all the mentioned statements are consistent with the observations made based on other diagrams and contours.

To examine the anisotropies of the set, a parameter is defined as the distribution function of the contact orientation $E(\theta)$ of the particle assembly that equals the total number of contacts in the angle range of $\theta \pm d\theta/2$ for angle increment $d\theta$. In addition to the contact orientation distribution function, distribution functions can also be defined for the average normal ($\bar{f}_n(\theta)$) and tangential ($\bar{f}_t(\theta)$) components of the contact forces between the particles. These so-called distribution functions can be written as [85]:

$$E(\theta) = 1/2\pi[1 + a\mathrm{Cos}2(\theta - \theta_a)] \tag{19}$$

$$\bar{f}_n(\theta) = \bar{f}_0[1 + a_n\mathrm{Cos}2(\theta - \theta_n)] \tag{20}$$

$$\bar{f}_t(\theta) = \bar{f}_0[-a_t\mathrm{Sin}2(\theta - \theta_t)] \tag{21}$$

where a, a^n, and a^t are the anisotropies of contact orientation and normal and tangential contact forces, respectively. In addition, θ^a is the principal direction of anisotropy, and θ^n and θ^t are the principal directions of the anisotropies of normal and tangential contact forces. Also, $\bar{f}_0$ is the average inter-particle contact force of the assembly. In Fig. 14,

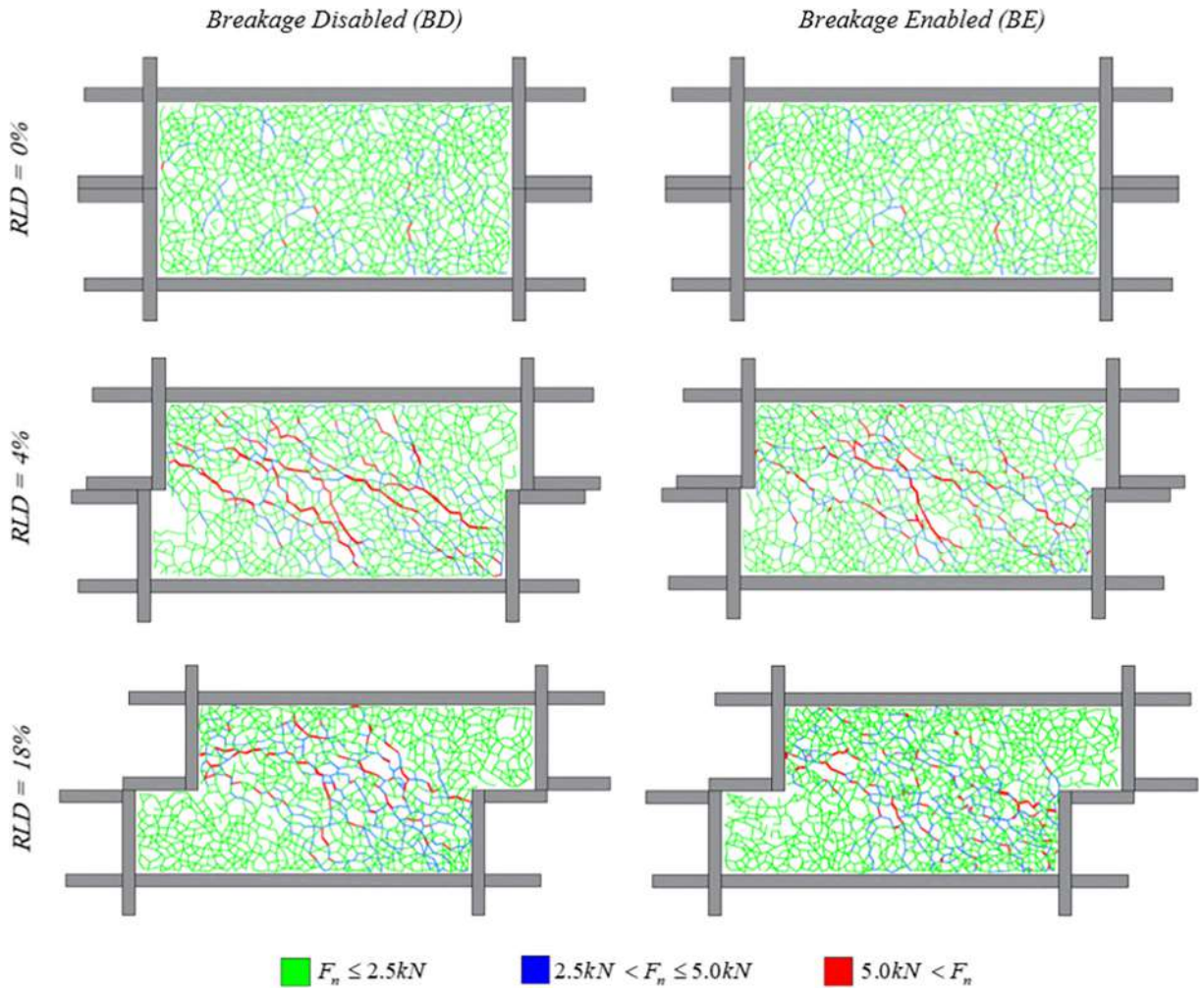

Fig. 13. Normal contact force chains (F_n) of both BD and BE assemblies during the lateral displacement phase of the direct shear test.

Fig. 15, and Fig. 16, polar histograms of the contact orientation and normal and tangential contact forces for both BD and BE samples are presented, respectively.

In fact, during the process of deformation in the particle assembly, new contacts were formed so that the concentration of the polar distribution of the contact orientation increased in line with the major principal compressive stress direction of the assembly. In other words, particles in a discrete media tried to transfer the applied stress to each other in the direction of the major principal compressive stress by forming a set of new contacts. As seen, the mentioned polar histograms represent a similar trend with the contact force chains of the assembly. Also, by comparing the assembly anisotropy in the presented polar histograms with those in the study of Naeij and Mirghasemi [2] on an assembly of elliptical particles under direct shear test, a good agreement is observed.

Table 4
Variation in the number of strong contact forces and assembly participation number during the test.

Relative lateral displacement (%)	Number of strong contact forces			Assembly participation number		
	0%	4%	18%	0%	4%	18%
Breakage disabled (BD)	24	302	243	0.62	0.43	0.45
Breakage enabled (BE)	24	292	201	0.62	0.48	0.52

As shown in Fig. 14 and Fig. 15, since the particle assembly was subjected to vertical stress before the lateral displacement phase, particles were moved toward each other vertically. Hence, a large number of contact force chains were formed in this direction; so, the distribution of contact orientation and normal contact forces were higher in the vertical direction. As the lateral displacement was applied, due to the increase in the number of inter-particle contacts and the value of horizontal contact forces, all of the mentioned histograms enlarged and rotated counterclockwise. At the RLD of 4%, the anisotropy of the particle assembly reached its peak, and the polar histograms of contact orientation and normal contact forces distributions took on a peanut shape. As the lateral displacement continued, the particle assembly anisotropy was gradually reduced, and the form of the aforesaid polar histograms became slightly more uniform.

According to Fig. 16, the tangential contact forces just before the lateral displacement phase were rather small; because at this stage, most inter-particle contacts were relatively normal. As a result, the size of the polar histograms of tangential contact forces and their Fourier expansions were extremely small at this step of the test. However, under hydrostatic stress conditions, if the number of particles is large enough and the stress distribution is fully isotropic, there are no tangential contact forces, and the polar histograms of tangential contact forces look almost like a dot. Nevertheless, in the present study, at the beginning of the lateral displacement phase, the assembly was under the desired vertical stress, so the mentioned histogram, despite its small size, was not similar to a dot. The value of tangential contact forces increased in

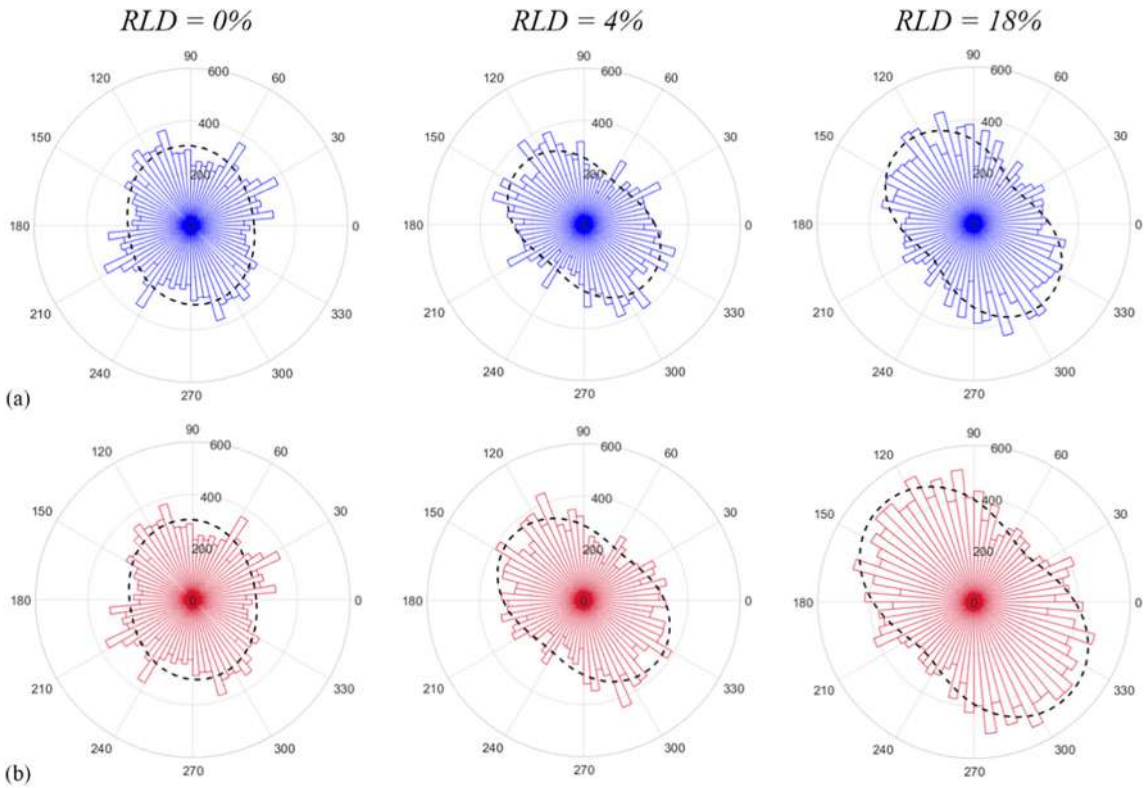

Fig. 14. Histogram of contact orientations during the lateral displacement phase of the direct shear test for: (a) the BD assembly; (b) the BE assembly.

both horizontal (0^o) and vertical (90^o) directions until the maximum shear strength point; and then decreased as the test continued. In other words, the value of tangential contact forces in the contacts with horizontal and vertical directions was significantly higher than the value of those in the diagonal direction contacts. The reason is that due to the applied lateral displacement, on the one hand, the large

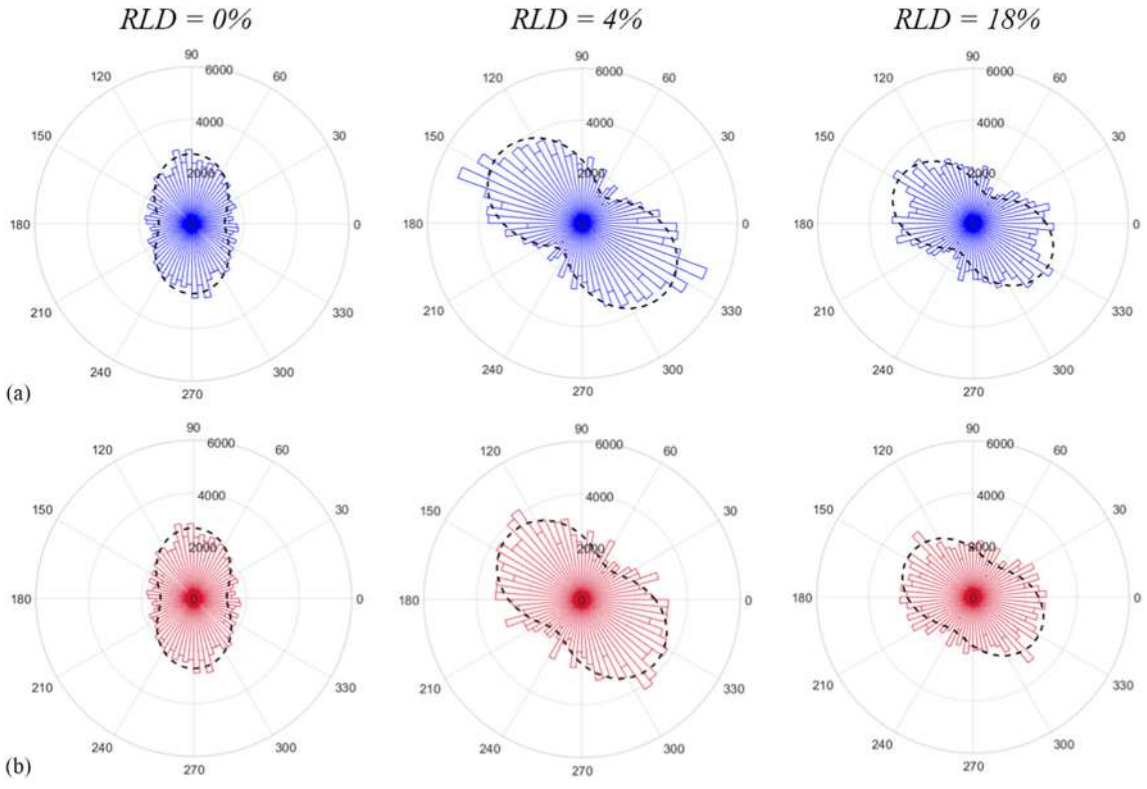

Fig. 15. Histogram of normal contact forces during the lateral displacement phase of the direct shear test for: (a) the BD assembly; (b) the BE assembly.

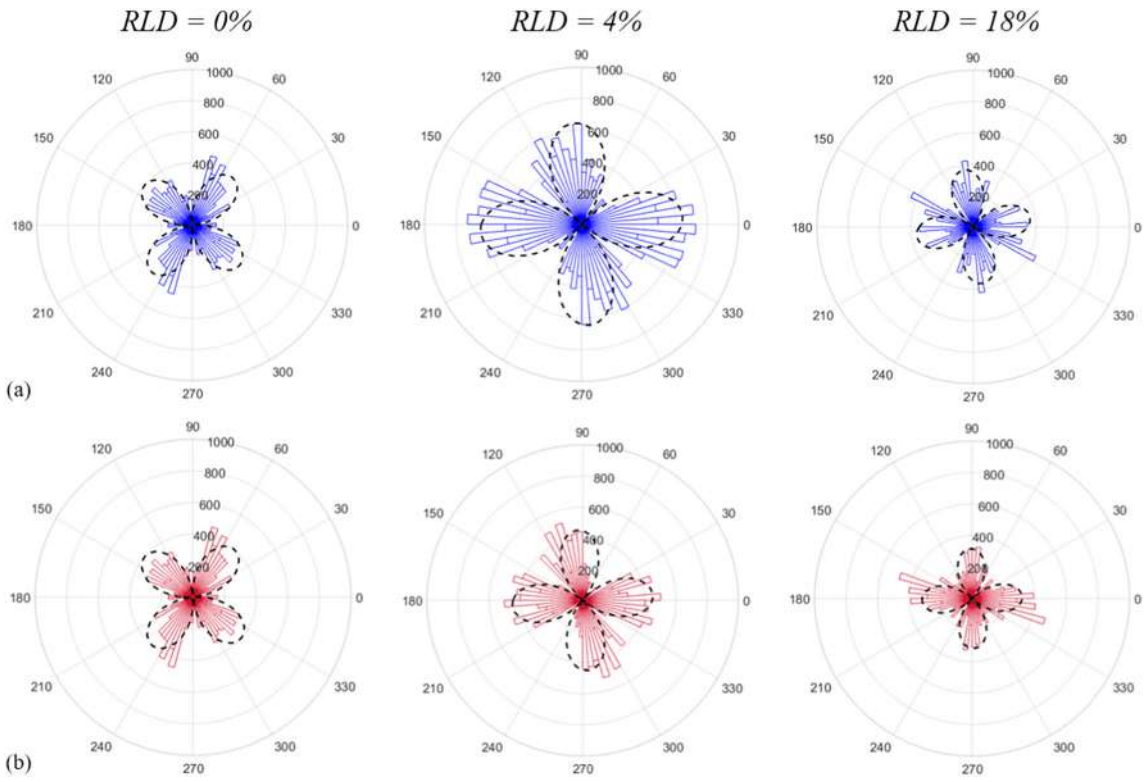

Fig. 16. Histogram of tangential contact forces during the lateral displacement phase of the direct shear test for: (a) the BD assembly; (b) the BE assembly.

number of strong NW-SE diagonal contacts (↘) had a relatively normal nature, and on the other hand, the contacts in line with the NE-SW diagonal direction (↗) were few in number and weak in amount compared to the contacts in line with the other diagonal direction (↘).

Fig. 17 presents the variation in the anisotropies and their principal directions for both BD and BE samples versus the RLD, during the test. As seen, by applying the lateral displacement to the assembly, the anisotropy of contact orientation (a) increased until the RLD of about 4%; then, a gradual slope drop can be observed in the aforementioned curve. Additionally, the anisotropy of normal contact forces (a_n) decreased after its upward trend in the first 4% RLD of the sample, owing to the collapse of strong force chains in line with the NW-SE diagonal direction (↘). Moreover, to explain the anisotropy of tangential contact forces (a_t) variation, it can be said that because of the high gradient of displacement in the shear band area at the early stages of the lateral loading, the internal friction between the particles was rapidly mobilized. However, as the dilation of the assembly began, the amount of interlocking and confinement in the area mentioned above, where most of the contacts with strong tangential components were formed, were reduced. Therefore, the anisotropy of tangential contact forces took on a descending trend after its initial rapid increase.

By comparing the BD and BE samples anisotropies, it can be seen that due to the particle breakage and the generation of new particles, new inter-particle contacts were formed in the BE assembly, which increased the total number of contacts in the sample. Additionally, this increase in the number of inter-particle contacts occurred in all directions, which led to a reduction in the assembly contact orientation anisotropy. Also, as the particle breakage broke down the strong normal contact force chains in the BE assembly, the values of normal contact forces in the NW-SE diagonal direction (↘) were reduced. Accordingly, by the reduction in the amount of difference in the average normal contact forces in line with the two diagonal directions, the assembly normal contact forces anisotropy decreased. Therefore, in this situation, the shape of the polar histograms resembled the capsule shape more than the peanut shape. In the same way, the particle breakage phenomenon removed the relatively strong tangential contact forces in the BE assembly, which were mostly caused by contacts in line with horizontal (0^o) and vertical (90^o) directions; then smaller tangential inter-particle contact forces were formed between the new broken particles; hence, the assembly tangential contact forces anisotropy was reduced as well.

As shown in Fig. 17, at the beginning of the lateral displacement phase, the principal directions of all of the anisotropies were about 90^o; at this stage, most of the inter-particle contacts were formed in the vertical direction to resist the vertical load. Nonetheless, as the relative lateral displacement increased to the point of maximum shear strength, these principal directions rotated counterclockwise to the diagonal direction (about 40^o). Subsequently, because of the increase in the number of vertical inter-particle contacts due to the dilative behavior of the assembly, the principal direction of the contact orientation anisotropy became slightly more vertical, which is less noticeable in the BE sample, given its lower dilative behavior. However, since the dilative behavior of the assembly reduced the values of the normal components of the vertical contact forces, the principal direction of the normal contact forces anisotropy tended to become a little more horizontal, which is also less noticeable in the BE sample. Moreover, the relatively constant principal direction of the tangential contact forces anisotropy increased slightly in the BE sample after the RLD of 4%, as the new inter-particle contacts formed in all directions.

In order to comprehend the force transmission in a discrete granular media from a microstructural perspective, the components of the average stress tensor of a particle assembly (σ_{ij}) can also be determined based on the above-mentioned anisotropies, as follows [6]:

$$\sigma_{11} = P[1 + 0.5aa_n \cos 2(\theta_a - \theta_n) + 0.5(a\cos(2\theta_a) + a_n \cos(2\theta_n) + a_t \cos(2\theta_t))] \quad (22)$$

$$\sigma_{22} = P[1 + 0.5aa_n \cos 2(\theta_a - \theta_n) - 0.5(a\cos(2\theta_a) + a_n \cos(2\theta_n) + a_t \cos(2\theta_t))] \quad (23)$$

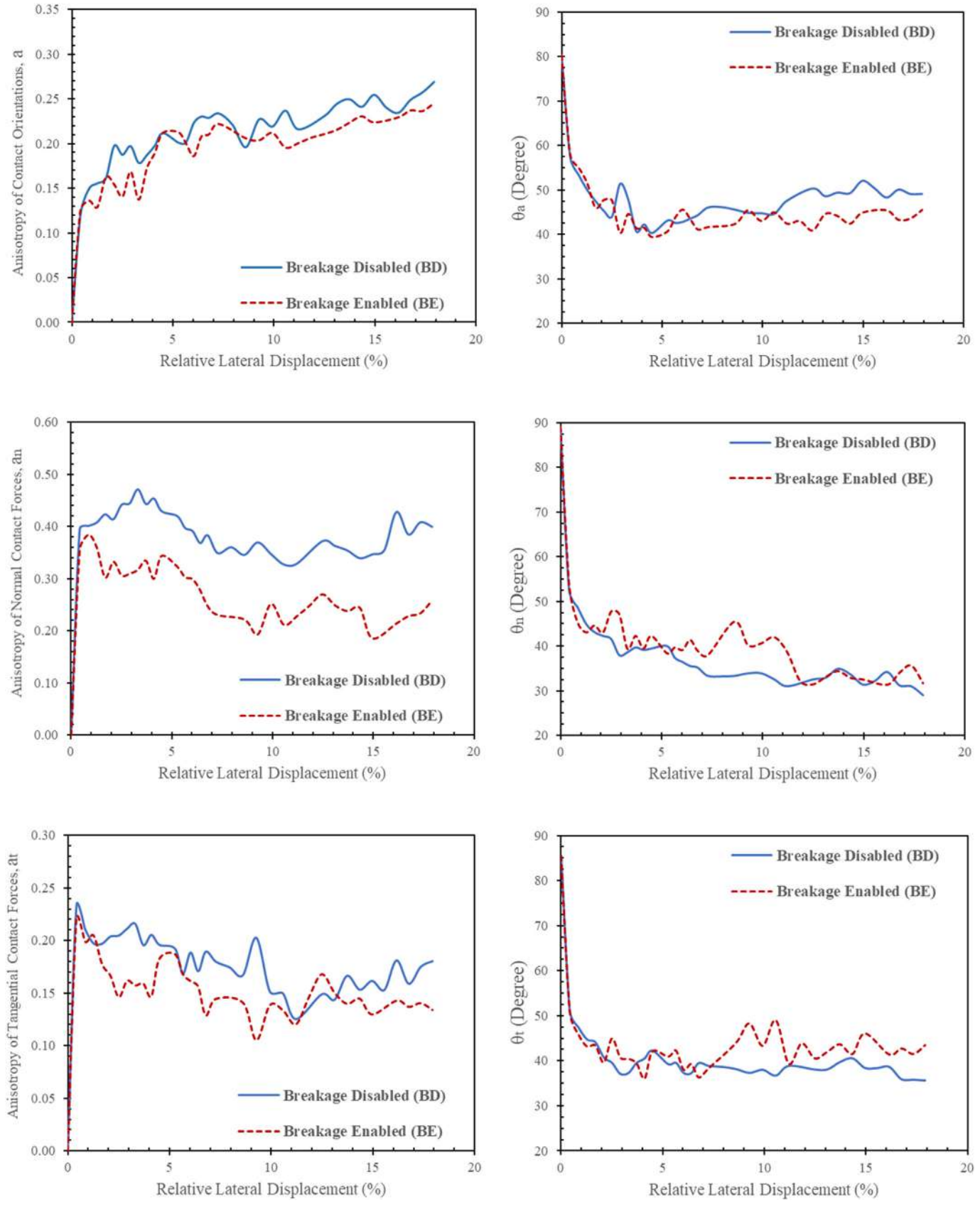

Fig. 17. Variation in the anisotropy and its principal direction of contact orientations, and normal and tangential contact forces of both BD and BE assemblies during the lateral displacement phase of the direct shear test.

$$\sigma_{12} = \sigma_{21} = P[0.5(a\sin(2\theta_a) + a_n \sin(2\theta_n) + a_t \sin(2\theta_t))] \quad (24)$$

$$P = 0.5 m_v \bar{l}_0 \bar{f}_0 \quad (25)$$

where the contact density m_v is the ratio of the total number of assembly contacts to the assembly area; also, $\overline{l_0}$ is the assembly average contact vector length.

After determining the components of the stress tensor, the stress tensor invariants (σ_n, σ_t) and the mobilized friction angle of the assembly (φ) can be obtained using the Mohr-Coulomb theory [85]:

$$\mathrm{Sin}(\varphi) = \frac{\sigma_t}{\sigma_n} = \frac{\sqrt{0.25(\sigma_{11}-\sigma_{22})^2 + {\sigma_{12}}^2}}{0.5(\sigma_{11}+\sigma_{22})} \quad (26)$$

Rothenburg and Bathurst [85], in their studies on the microstructure of granular media, assumed that all of the three principal directions of the anisotropy of contact orientation and normal and tangential contact forces are coincident (i.e., $\theta_a = \theta_n = \theta_t$). Conversely, Wang et al. [6] demonstrated that the previous assumption of coincident principal directions is not entirely valid for a particle assembly in the direct shear test. According to *Rothenburg* and *Bathurst* [85], Eq. (26) can be modified as Eq. (27). Rothenburg and Bathurst [86] also proposed a simplified equation for *Sin(φ)* by neglecting the term $0.5aa_n$ in the denominator of the previous equation because of its small value.

$$\mathrm{Sin}(\varphi) = \frac{0.5(a + a_n + a_t)}{(1 + 0.5a\, a_n)} \simeq 0.5(a + a_n + a_t) \quad (27)$$

Following the determination of the assembly mobilized friction angle from the microstructural perspective, *Sin(φ)* can also be obtained from the macro-mechanical measurements, as follows:

$$\mathrm{Sin}(\varphi) = \frac{\sigma_1 - \sigma_2}{\sigma_1 + \sigma_2} \quad (28)$$

where the σ_1 and σ_2 are the major and minor principal stresses of the assembly, respectively.

Fig. 18 represents a comparison between the macro- and micro-mechanical mobilized friction angles of both BD and BE assemblies. According to the correspondence between the variation trends of all calculated friction angles, it can be declared that the mobilized friction angle of a particle assembly, on which the assembly macro-mechanical behavior mostly depends, is directly under the influence of its anisotropies. In addition, from the macro- and micro-mechanical curve correspondence point of view, it can be said that the friction angle calculated using the suggestions of Wang et al. [6] is more precise than the determined friction angle of Rothenburg and Bathurst [85]; furthermore, the friction angle obtained from the simplified equation of Rothenburg and Bathurst [85] is moderately overestimated. By comparing the mobilized friction angles of the BD and BE samples in Fig. 18, it is found that the occurrence of particle breakage, which reduced the assembly anisotropy and the interlocking between the particles, decreased the assembly mobilized friction angle.

6. Summary and conclusions

The present study numerically simulated the assemblies of breakable angular particles using a combined DEM-XFEM novel model to investigate the macro- and micro-mechanical behavior of rockfills under the direct shear test. In addition, to study the effect of particle breakage phenomenon on the mechanical behavior of these granular materials, the results from the simulation of a breakage-disabled (BD) sample and a breakage-enabled (BE) one were examined and compared from different macrostructural and microstructural aspects. The main findings were:

- The distribution of broken particles in the shear box had a diagonal trend. Additionally, there was a significantly higher frequency of broken particles in the middle third of the shear box.
- The relatively smaller particles generated from the breakage of the initial ones filled the existing pore spaces of the set and moved in step with their adjacent particles, which reduced the assembly dilative behavior and the particles interlocking.
- The trend of horizontal and vertical particle displacements of the sample with particle breakage was more uniform than that of the other sample.
- The number of particles under high stresses and the overall stress state of the assembly decreased due to the particle breakage occurrence. Additionally, most of the strong contact force chains formed in the NW-SE diagonal direction of the shear box (↘), collapsed in the BE assembly.
- Particle breakage reduced the assembly anisotropies, and since the macro-mechanical behavior of granular materials depends on their microstructure, the mobilized friction angle of the BE assembly was lower than that of the BD one.

Overall, the results confirmed that the developed DEM-XFEM approach could adequately simulate direct shear tests on granular materials composed of breakable angular particles and demonstrate particle breakage effects on their mechanical behavior.

Declaration of Competing Interest

The authors declare that they have no known competing financial interests or personal relationships that could have appeared to influence the work reported in this paper.

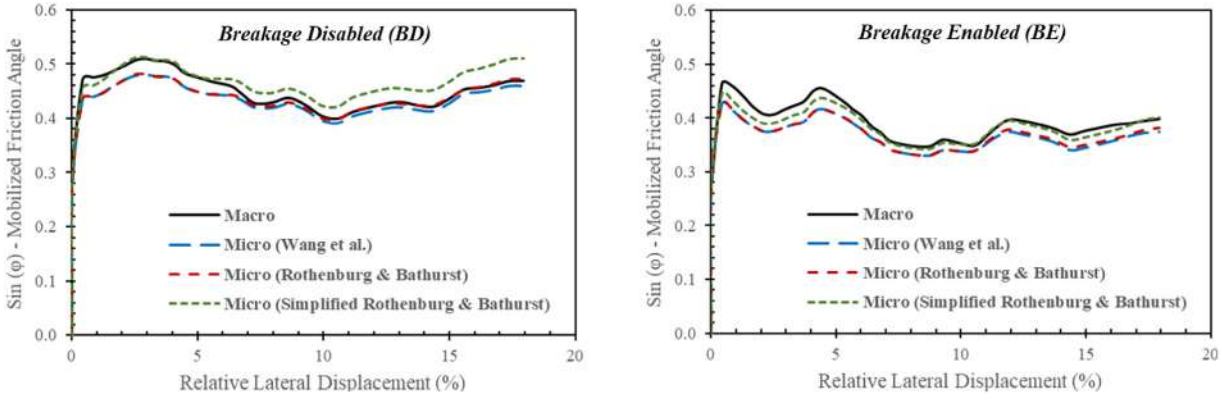

Fig. 18. Variation in the mobilized friction angles of both BD and BE assemblies during the lateral displacement phase of the direct shear test.

References

[1] K. Terzaghi, R. Peck, Soil Mechanics in Engineering Practice, John Wiley, New York, 1948.
[2] M. Naeij, Investigation of the Anisotropy Coefficients Changes of a Particle Assembly in Direct Shear Test Using DEM, University of Tehran, 2011.
[3] N. Morgenstern, J. Tchalenko, Microscopic structure in kaolin subjected to direct shear, Geotechnique 4 (1976) 309–328.
[4] S.H. Liu, D. Sun, H. Matsuoka, On the interface friction in direct shear test, Comput. Geotech. 32 (2005) 317–325.
[5] L. Zhang, C. Thornton, A numerical examination of the direct shear test, Géotechnique 57 (2007) 343–354.
[6] J. Wang, J.E. Dove, M.S. Gutierrez, Discrete-continuum analysis of shear banding in the direct shear test, Géotechnique 57 (2007) 513–526.
[7] Q. Zhou, H.H. Shen, B.T. Helenbrook, H. Zhang, Scale dependence of direct shear tests, Sci. Bull. (Beijing) 54 (2009) 4337–4348.
[8] L. Cui, C. O'Sullivan, Exploring the macro- and micro-scale response of an idealised granular material in the direct shear apparatus, Géotechnique 56 (2006) 455–468.
[9] J.M. Ting, M. Khwaja, L.R. Meachum, J.D. Rowell, An ellipse-based discrete element model for granular materials, Int. J. Numer. Anal. Methods Geomech. 17 (1993) 603–623.
[10] A. Bagherzadeh-Khalkhali, A.A. Mirghasemi, Numerical and experimental direct shear tests for coarse-grained soils, Particuology 7 (2009) 83–91.
[11] A.A. Mirghasemi, M. Naeij, The effect of initial elongation of elliptical particles on macro – micromechanical behavior during direct shear test, Proc. Eng. 102 (2015) 1476–1483.
[12] W.M. Yan, Fabric evolution in a numerical direct shear test, Comput. Geotech. 36 (2009) 597–603.
[13] Y. Yan, S. Ji, Discrete element modeling of direct shear tests for a granular material, Int. J. Numer. Anal. Methods Geomech. 34 (2010) 978–990.
[14] W.-J. Xu, S. Wang, H.-Y. Zhang, Z.-L. Zhang, Discrete element modelling of a soil-rock mixture used in an embankment dam, Int. J. Rock Mech. Min. Sci. 86 (2016) (1997) 141–156.
[15] S.P.K. Kodicherla, G. Gong, Z.X. Yang, K. Krabbenhoft, L. Fan, C.K.S. Moy, S. Wilkinson, The influence of particle elongations on direct shear behaviour of granular materials using DEM, Granul. Matter. 21 (2019) https://doi.org/10.1007/s10035-019-0947-x.
[16] A. Danesh, A.A. Mirghasemi, M. Palassi, Evaluation of particle shape on direct shear mechanical behavior of ballast assembly using discrete element method (DEM), Transp. Geotech. 23 (2020) 100357.
[17] H. Bayesteh, A.A. Mirghasemi, Numerical simulation of pore fluid characteristic effect on the volume change behavior of montmorillonite clays, Comput. Geotech. 48 (2013) 146–155.
[18] M. Khabazian, A.A. Mirghasemi, H. Bayesteh, Compressibility of montmorillonite/kaolinite mixtures in consolidation testing using discrete element method, Comput. Geotech. 104 (2018) 271–280.
[19] K.A. Jaradat, S.L. Abdelaziz, On the use of discrete element method for multi-scale assessment of clay behavior, Comput. Geotech. 112 (2019) 329–341.
[20] M. Khabazian, A.A. Mirghasemi, H. Bayesteh, Discrete-element simulation of drying effect on the volume and equivalent effective stress of kaolinite, Géotechnique (2020) 1–13.
[21] A. Bagherzadeh-Khalkhali, A.A. Mirghasemi, S. Mohammadi, Micromechanics of breakage in sharp-edge particles using combined DEM and FEM, Particuology 6 (2008) 347–361.
[22] A. Bagherzadeh, A.A. Mirghasemi, S. Mohammadi, Numerical simulation of particle breakage of angular particles using combined DEM and FEM, Powder Technol. 205 (2011) 15–29.
[23] G. Ma, W. Zhou, X.-L. Chang, Modeling the particle breakage of rockfill materials with the cohesive crack model, Comput. Geotech. 61 (2014) 132–143.
[24] M. Michael, F. Vogel, B. Peters, DEM–FEM coupling simulations of the interactions between a tire tread and granular terrain, Comput. Methods Appl. Mech. Eng. 289 (2015) 227–248.
[25] T. Luo, E.T. Ooi, A.H.C. Chan, S.J. Fu, The combined scaled boundary finite-discrete element method: grain breakage modelling in cohesion-less granular media, Comput. Geotech. 88 (2017) 199–221.
[26] J. Raisianzadeh, A.A. Mirghasemi, S. Mohammadi, 2D simulation of breakage of angular particles using combined DEM and XFEM, Powder Technol. 336 (2018) 282–297.
[27] J. Raisianzadeh, S. Mohammadi, A.A. Mirghasemi, Micromechanical study of particle breakage in 2D angular rockfill media using combined DEM and XFEM, Granul. Matter. 21 (2019) https://doi.org/10.1007/s10035-019-0904-8.
[28] T. Foroutan, A.A. Mirghasemi, CFD-DEM model to assess stress-induced anisotropy in undrained granular material, Comput. Geotech. 119 (2020) 103318.
[29] Z. Hu, Z.X. Yang, Y.D. Zhang, CFD-DEM modeling of suffusion effect on undrained behavior of internally unstable soils, Comput. Geotech. 126 (2020) 103692.
[30] R.J. Marsal, Large-scale testing of rockfill materials, Journal of the Soil Mechanics and Foundations Division. 93 (1967) 27–43.
[31] P.V. Lade, J.A. Yamamuro, Undrained sand behavior in axisymmetric tests at high pressures, J. Geotech. Eng. 122 (1996) 120–129.
[32] J.A. Yamamuro, P.V. Lade, Drained sand behavior in axisymmetric tests at high pressures, J. Geotech. Eng. 122 (1996) 109–119.
[33] P.V. Lade, J.A. Yamamuro, P.A. Bopp, Significance of particle crushing in granular materials, J. Geotech. Eng. 122 (1996) 309–316.
[34] A. Varadarajan, K.G. Sharma, K. Venkatachalam, A.K. Gupta, Testing and modeling two rockfill materials, J. Geotech. Geoenviron. Eng. 129 (2003) 206–218.
[35] A. Khonji, A. Bagherzadeh-Khalkhali, A. Aghaei-Araei, Experimental investigation of rockfill particle breakage under large-scale triaxial tests using five different breakage factors, Powder Technol. 363 (2020) 473–487.
[36] G.R. McDowell, O. Harireche, Discrete element modelling of soil particle fracture, Géotechnique 52 (2002) 131–135.
[37] Y.P. Cheng, M.D. Bolton, Y. Nakata, Crushing and plastic deformation of soils simulated using DEM, Géotechnique 54 (2004) 131–141.
[38] E. Oñate, J. Rojek, Combination of discrete element and finite element methods for dynamic analysis of geomechanics problems, Comput. Methods Appl. Mech. Eng. 193 (2004) 3087–3128.
[39] M.D. Bolton, Y. Nakata, Y.P. Cheng, Micro- and macro-mechanical behaviour of DEM crushable materials, Géotechnique 58 (2008) 471–480.
[40] J.E. Andrade, K.-W. Lim, C.F. Avila, I. Vlahinić, Granular element method for computational particle mechanics, Comput. Methods Appl. Mech. Eng. 241–244 (2012) 262–274.
[41] G.R. McDOWELL, J.P. de Bono, On the micro mechanics of one-dimensional normal compression, Géotechnique 63 (2013) 895–908.
[42] J.P. de Bono, G.R. McDowell, D. Wanatowski, DEM of triaxial tests on crushable cemented sand, Granul. Matter 16 (2014) 563–572.
[43] J. Wang, H. Yan, On the role of particle breakage in the shear failure behavior of granular soils by DEM, Int. J. Numer. Anal. Methods Geomech. 37 (2013) 832–854.
[44] T. Ueda, T. Matsushima, Y. Yamada, DEM simulation on the one-dimensional compression behavior of various shaped crushable granular materials, Granul. Matter 15 (2013) 675–684.
[45] E. Seyedi Hosseininia, A.A. Mirghasemi, Numerical simulation of breakage of two-dimensional polygon-shaped particles using discrete element method, Powder Technol. 166 (2006) 100–112.
[46] E. Seyedi Hosseininia, A.A. Mirghasemi, Effect of particle breakage on the behavior of simulated angular particle assemblies, China Particuol. 5 (2007) 328–336.
[47] P. Wang, Z. Karatza, C. Arson, DEM modelling of sequential fragmentation of zeolite granules under oedometric compression based on XCT observations, Powder Technol. 347 (2019) 66–75.
[48] J.M. Harmon, D. Arthur, J.E. Andrade, Level set splitting in DEM for modeling breakage mechanics, Comput. Methods Appl. Mech. Eng. 365 (2020) 112961.
[49] F. Dastjerdy, O.R. Barani, F. Kalantary, Modeling of hydraulic fracture problem in partially saturated porous media using cohesive zone model, Int. J. Civ. Eng. 13 (2015) 185–194.
[50] O.R. Barani, S. Majidaie, M. Mosallanejad, Numerical modeling of water pressure in propagating concrete cracks, J. Eng. Mech. 142 (2016), 04016011.
[51] O.R. Barani, M. Mosallanejad, S.A. Sadrnejad, Fracture analysis of cohesive soils using bilinear and trilinear cohesive laws, Int. J. Geomech. 16 (2016), 04015088.
[52] S.M. Seyyedan, O.R. Barani, Cohesive crack model for fiber reinforced cemented sands, 6th European Conference on Computational Mechanics (ECCM 6) and 7th European Conference on Computational Fluid Dynamics (ECFD 7), Glasgow, UK, 2018 http://congress.cimne.com/eccm_ecfd2018/admin/files/filePaper/p1169.pdf.
[53] O.R. Barani, M. Bahrami, S.A. Sadrnejad, A new finite element for back analysis of a geogrid reinforced soil retaining wall failure, Int. J. Civ. Eng. 16 (2018) 435–441.
[54] S. Mohammadi, Extended Finite Element Method: For Fracture Analysis of Structures, Wiley-Blackwell, Chichester, England, 2007.
[55] S. Mohammadi, XFEM Fracture Analysis of Composites: Mohammadi/XFEM Fracture Analysis of Composites, John Wiley & Sons, Ltd, Chichester, UK, 2012.
[56] F. Zhu, J. Zhao, Interplays between particle shape and particle breakage in confined continuous crushing of granular media, Powder Technol. 378 (2021) 455–467.
[57] E. Hoek, Strength of jointed rockmasses, Geotechnique 33 (1983) 187–223.
[58] J. Zuo, J. Shen, The Hoek-Brown Failure Criterion-from Theory to Application, 1st ed. Springer, Singapore, Singapore, 2021.
[59] A.A. Mirghasemi, L. Rothenburg, E.L. Matyas, Numerical simulations of assemblies of two-dimensional polygon-shaped particles and effects of confining pressure on shear strength, Soils Found. 37 (1997) 43–52.
[60] A.A. Mirghasemi, L. Rothenburg, E.L. Matyas, Influence of particle shape on engineering properties of assemblies of two-dimensional polygon-shaped particles, Géotechnique 52 (2002) 209–217.
[61] A. Zang, O. Stephansson, Stress Field of the Earth's Crust, Springer Netherlands, Dordrecht, 2010.
[62] M.K. Samal, M. Seidenfuss, E. Roos, A comparative assessment of local and nonlocal damage models for prediction of fracture behavior during mixed-mode loading, Proc. Eng. 55 (2013) 493–498.
[63] J.D. Eshelby, The continuum theory of lattice defects, Solid State Physics, Elsevier 1956, pp. 79–144.
[64] J.D. Eshelby, The calculation of energy release rates, Prospects of Fracture Mechanics, Springer Netherlands, Dordrecht 1974, pp. 69–84.
[65] J.R. Rice, G.F. Rosengren, Plane strain deformation near a crack tip in a power-law hardening material, J. Mech. Phys. Solids 16 (1968) 1–12.
[66] F.Z. Li, C.F. Shih, A. Needleman, A comparison of methods for calculating energy release rates, Eng. Fract. Mech. 21 (1985) 405–421.
[67] H. Westergaard, Bearing pressures and cracks, J. Appl. Mech. 6 (1939) 49–53.
[68] V.E. Saouma, Fracture Mechanics. Lecture Notes, CVEN-6831, University of Colorado, USA, 2000.
[69] F. Erdogan, G.C. Sih, On the crack extension in plates under plane loading and transverse shear, J. Basic Eng. 85 (1963) 519–525.
[70] G.R. Irwin, Analysis of stresses and strains near the end of a crack traversing a plate, J. Appl. Mech. 24 (1957) 361–364.
[71] A.S.T.M. D3967-08, Standard Test Method for Splitting Tensile Strength of Intact Rock Core Specimens, ASTM International, West, Conshohocken, PA, USA, 2008.
[72] D. Li, L.N.Y. Wong, The Brazilian disc test for rock mechanics applications: review and new insights, Rock Mech. Rock. Eng. 46 (2013) 269–287.

[73] M. Mellor, I. Hawkes, Measurement of tensile strength by diametral compression of discs and annuli, Eng. Geol. 5 (1971) 173–225.
[74] M.A. Perras, M.S. Diederichs, A review of the tensile strength of rock: concepts and testing, Geotech. Geol. Eng. 32 (2014) 525–546.
[75] E. Hoek, E.T. Brown, Practical estimates of rock mass strength, Int. J. Rock Mech. Min. Sci. 34 (1997) (1997) 1165–1186.
[76] D.U. Deere, in: K.G. Stagg, O.C. Zienkiewicz (Eds.), Chapter 1: Geological Considerations, John Wiley and Sons, London 1968, pp. 1–20.
[77] A. Palmström, R. Singh, The deformation modulus of rock masses—comparisons between in situ tests and indirect estimates, Tunn. Undergr. Space Technol. 16 (2001) 115–131.
[78] E. Hoek, Practical Rock Engineering, Available online http://www.rockscience.com 2000.
[79] Z.X. Zhang, An empirical relation between mode I fracture toughness and the tensile strength of rock, Int. J. Rock Mech. Min. Sci. 39 (2002) (1997) 401–406.
[80] A.S.T.M. D3080-04, Standard Test Method for Direct Shear Test of Soils Under Consolidated Drained Conditions, ASTM International, West, Conshohocken, PA, USA, 2004.
[81] A. Danesh, M. Palassi, A.A. Mirghasemi, et al., Granul. Matter. 20 (2018) https://doi.org/10.1007/s10035-018-0824-z.
[82] S. Shahrokhi, O.R. Barani, Coupled directional dilation–damage approach to model the cyclic-undrained response of soft clay under pure principal stress axes rotation, J. Eng. Mech. 146 (2020), 04020033.
[83] H.P. Zhang, H.A. Makse, Jamming transition in emulsions and granular materials, Phys. Rev. E Stat. Nonlinear Soft Matter Phys. 72 (2005), 011301.
[84] X. Deng, R.N. Davé, Properties of force networks in jammed granular media, Granul. Matter. 19 (2017) https://doi.org/10.1007/s10035-017-0715-8.
[85] L. Rothenburg, R.J. Bathurst, Analytical study of induced anisotropy in idealized granular materials, Géotechnique 39 (1989) 601–614.
[86] L. Rothenburg, R.J. Bathurst, Micromechanical features of granular assemblies with planar elliptical particles, Géotechnique 42 (1992) 79–95.